

# Accretion and inter-cycle variations in the PMS interacting binary AK Sco

Ana I. Gómez de Castro<sup>1,2</sup>, Juan Carlos Vallejo<sup>1,2</sup>, Ada Canet-Varea<sup>1,2</sup>, Parke Loyd<sup>3</sup>, Kevin France<sup>4</sup>

Ana I. Gómez de Castro, Juan Carlos Vallejo, Ada Canet-Varea

[1] Joint Center for Ultraviolet Astronomy, Universidad Complutense de Madrid, Spain

[2] U.D. Astronomia y Geodesia, Fac. CC Matemáticas, Universidad Complutense de Madrid, Spain

Parke Loyd

[3] School of Earth and Space Exploration, Arizona State University, Tempe, AZ 85287 U.S.A.

Kevin France

[4] Laboratory for Atmospheric and Space Physics, University of Colorado, Boulder, CO 80309 U.S.A.

Received \_\_\_\_\_; accepted \_\_\_\_\_

## ABSTRACT

There are only a handful of known short-period pre-main sequence spectroscopic binaries with significant accretion rates (Class II sources). AK Sco stands out in this list because the system is composed of two equal mass F5 stars in a highly eccentric orbit thus both stars get as close as 11 stellar radii at periastron passage. This configuration is optimal for accretion studies because enhance accretion events can be precisely timed at periastron passage. In this work, we present the results from the monitoring of the AK Sco system with Hubble during three consecutive periastron passages. These data provide a unique dataset to spectroscopically characterize accretion and evaluate the inter-cycle variability of the system. Clear evidence of accretion rate enhancement was observed in cycle 1 and 3: the blueing of the near UV continuum, the sudden flux increase of important accretion tracers, such as the N V, Si IV and C IV lines, and also of neutral/singly ionized species such as O I and C II. Also, variations in the Si III]/C III] ratio reveals an enhancement of the electron density by an order of magnitude during the periastron passage. Moreover, in cycle 3, the spectral resolution of the observations obtained with the Cosmic Origins Spectrograph enabled discerning that the flow was channelled preferentially into one of the two components. The most remarkable feature in the cycle-to-cycle variations was the detection of a notable increase of the UV flux from cycle 1 to 2 that was not accompanied by enhanced accretion signatures.

*Subject headings:* stars: pre-main sequence, stars: magnetic fields

## 1. Introduction

Understanding the connection between accretion and outflow during pre-main sequence (PMS) evolution is a major endeavor in stellar astrophysics and it is required to understand planetary systems formation. The high energy spectrum (UV to X-ray) produced through accretion plays a key role in the photoevaporation of the gas in the young planetary disks (see Clarke, 2011 and Alexander et al. 2014 for recent reviews) setting the transition between the accreting Class II sources and the weak line T Tauri (WTTS) phase. There are plenty of studies both from the theoretical and observational point of view addressing this process (e.g. Hollenbach et al. 1994, Font et al. 2004, Alexander et al. 2004b, Gorti & Hollenbach 2009, Ercolano et al. 2009). There is however, a need for observations of close binary systems where tidal forces are very significant in the transport of angular momentum hence, in tapping the accretion flow. An additional source of interest relates with the formation and evolution of exoplanetary systems hosting the so-called hot Jupiters; close binaries with low mass ratio<sup>1</sup>, such as UZ Tau, provide important clues on giant planets formation and migration.

Most of the PMS-spectroscopic binaries (PMS-SBs) are low mass systems with primary spectral type G0 or later. In general, the known PMS-SBs are rather evolved objects containing very active young stars (WTTSs) surrounded by thin disks, often debris disks (see Melo et al. 2001 and Gómez de Castro & Marcos-Arenal 2015 for a recent compilation). There are only a handful of PMS-SB that belong to Class II, namely V4046 Sgr, AK Sco, DQ Tau, UZ Tau E with orbital period smaller than 20 days, GW Ori with period 241.9 days and CS Cha with period longer than 2482 days (Guenther et al. 2007). AK Sco stands out in this compilation because the system is composed of two equal mass F5 stars in a

---

<sup>1</sup>The mass ratio,  $q$ , is defined as  $q = M_2/M_1$ , being  $M_1$ , the mass of the primary and  $M_2$ , the mass of the secondary.

highly eccentric orbit ( $e=0.47$ ) that get as close as 11 stellar radii at periastron passage (Alencar et al. 2003). In PMS close binary systems, accretion disks can either take up or release angular momentum and the details of the evolution depend on the mass ratio between the two stars and on the orbit eccentricity (Artymowicz & Lubow, 1994; Bate & Bonnell, 1997; Hanawa et al 2010, de Val-Borro et al 2011, Shi et al. 2012). In particular, AK Sco’s highly eccentric orbit favors the formation of spiral waves within the inner disk; the variable gravitational potential produced by the binary acts as a gravitational piston that drags material efficiently from the inner border of the disk at apastron to release it onto the stars preferentially at periastron (see Figure 1, from Gómez de Castro et al. 2013, hereafter Paper I). Observational confirmation to this prediction has been provided recently by a Hubble monitoring campaign with the Cosmic Origins Spectrograph (COS) (Gómez de Castro et al. 2016, hereafter Paper II); coincident with periapsis, a marked 10% decrease in the  $H_2$  emission from the disk was detected caused by an infalling filament of gas that absorbs the stellar  $Ly\alpha$  photons and shades some of the  $H_2$  molecules on the disk surface. The light curves also showed an associated enhancement of the main accretion tracers, namely, C IV, Si IV, N V, C III, Si III resonance UV multiplets (Paper II). AK Sco was also monitored for two more cycles with the Space Telescope Imaging Spectrograph (STIS). All together, the data acquired during these three consecutive cycles provide a unique dataset to spectroscopically characterize accretion and evaluate the inter-cycle variability of the system. The aim of this work is to present the results of this analysis.

The article is organized as follows. A comprehensive summary of the Hubble observing campaign is provided in Section 2. AK Sco was monitored during the first two cycles with the Space Telescope Imaging Spectrograph (STIS) providing low dispersion, high sensitivity spectra in the full 1140 Å - 3184 Å spectral range; the results from this STIS-based monitoring are described in Section 3. During the last cycle, AK Sco was monitored with COS in the 1159 Å - 1762 Å range with much better spectral dispersion (19,000) to study

the kinematics of the line emitting plasma and resolve properly the H<sub>2</sub> emission features. The main results from this cycle are gathered in Paper II however, the detailed description of the kinematics of the radiating plasma is included in Section 4. In Section 5, the data from all the three cycles are analyzed together and compared with the predictions from numerical simulations of the dynamical evolution of the binary. STIS data also show evidence of an extended diffuse envelope around the system radiating in Ly $\alpha$  as will be shown in Section 6. All observations were obtained in photon counting mode, this enabled studying in detail the light curves especially, during the long COS observations. The analysis is included in Section 7 and shows no evidence for short time scale fluctuations ( $\tau \leq 800$  s) neither in the C IV light curve nor in the overall far UV spectrum. To conclude, a short summary with the main results is in Section 8.

## 2. Observing program and spectral overview

The observations were obtained in July-August 2014 with the instruments Space Telescope Imaging Spectrograph (STIS) and Cosmic Origins Spectrograph (COS), the log of observations is in Table 2. As shown in Fig. 2, AK Sco was tracked during periastron passage in three consecutive periods. During the first two periods, it was observed in low dispersion with STIS and gratings G140L and G230L, to get full coverage in the range: 1140 Å – 3184 Å range with high sensitivity and spatial information. In the last period only the 1159 Å – 1762.490 Å range was observed but with higher dispersion (19,000) using the gratings G130M and G160M in COS. Observations were carried out in photon counting mode to preserve as much temporal information as possible and enable the time series analysis of the results.

The average spectrum of AK Sco during the observing run is displayed in Fig. 3. Emission lines formed at a broad range of plasma temperatures are detected as otherwise,

usually observed in the ultraviolet spectrum of the T Tauri stars (TTs) (Gómez de Castro, 2009): emission from  $H_2$  molecular bands, from the resonance transitions of highly ionized species (N V, C IV, Si IV), intermediate ionization species (C III, Si III, O III) and singly ionized or neutral plasma (C I, C II, O I, O II, Mg II, Si II, Fe II). Contributions from the stellar atmosphere, the outflow and the accretion flow are expected in all of them. The unique feature about Fig. 3 is the unprecedented SNR of the UV continuum obtained after co-adding all exposures. In Fig. 4, the reddening corrected average spectrum ( $A_V = 0.5$ ,  $R = 4.3$ , see Table 1) is compared with that of the nearby F-type main sequence stars, HD 139664 and HD 22879 (see Appendix A for details on the UV spectrum of F stars). HD 139664 (F5) is known to have a debris disk but thin enough to have a tiny contribution to the infrared IRAS flux (see Fig. 8 in Scheneider et al. 2014). Some of the main photospheric features of an F5 star are readily recognized in AK Sco UV spectrum, as well as the significant excess below 2000 Å. The overall UV spectral energy distribution is closer to a later spectral type (F9) star than to an F5.

### 3. Results from the STIS monitoring

#### 3.1. UV Continuum variability

The UV continuum of F stars in the 1640 – 3100 Å is very sensitive to the spectral type, as shown in detail in Appendix A. This trend is quantified in Fig. 5 where the ratio between the integrated fluxes in the bands: F1 (1640 – 2400 Å), F2 (2400 – 2775 Å) and F3 (2830 – 3100 Å) has been computed for the F stars in Table A1 and used to build the rates  $R1 = F1/F2$  and  $R2 = F2/F3$  represented in the Figure. Spectral types of main sequence stars are indicated, they define a clear trend parallel to the extinction arrow; extinction is negligible for most of them (see Table A1). Each band traces a main component: F1 is the most significantly affected by extinction (also includes the UV bump),

F2 is dominated by the Fe II multiplets and F3 by the Balmer continuum and the stellar photosphere. The 55 Å separation between F2 and F3 bands has been set to avoid the very strong Mg II feature. The extinction arrow has been drawn for the average ISM extinction law (Fitzpatrick & Massa, 2007), as well for a modified extinction law with  $R = 4.3$  that according to Manset et al. (2005) is representative of the circumstellar environment in AK Sco. Notice that the extinction arrow runs roughly parallel to the spectral types, i.e., there is degeneracy between spectral type and extinction.

We have computed  $R1$  and  $R2$  for all STIS observations of AK Sco (cycles 1 and 2) and over-plotted them on the figure. AK Sco is located closer to late F stars than to early F in the diagram though it is classified as an F5 star from its optical spectrum. AK Sco extinction is small,  $A_V = 0.5$  (see Table 1) or  $E(B-V) \simeq 0.12$ , and thus extinction alone cannot account for the observed SED. Henceforth, according to its UV spectrum, AK Sco should be classified as an F8-F9 star instead of the F5 type assigned on the base of its optical spectrum. Moreover, the excess contribution from the accretion flow pushes AK Sco away from the main sequence band. The variations found during our observing campaign go basically perpendicular to the extinction arrow and are most likely caused by variations in the accretion rate. The integrated UV flux in the 1640 – 3100 Å spectral range increased by a 17% from cycle 1 to cycle 2.

During cycle 1, the excursion of AK Sco in the diagram has a non-negligible component parallel to the extinction arrow of  $E(B - V) \simeq 0.01$ , corresponding to a variation in  $A_V$  of -0.043 ( $A_V = R * E(B - V)$ ); this variation is towards a decreasing extinction or increasing blueing of the spectrum in the middle of the cycle’s observations.

### 3.2. Spectral lines variability

In figure 6, the spectral variability during cycle 1 and 2 is represented. The variability has been computed as the standard deviation of the mean of the spectra for each cycle<sup>2</sup>; as displayed it is concentrated in the cores of the emission lines but there are differences between both cycles, being the main,

- The variability of the most prominent UV lines is a factor of 2 higher during cycle 1 than during cycle 2.
- During cycle 1, the UV continuum (2630 Å - 3150 Å ) varies by less than 0.8%; during cycle 2 this variation rises to 2.2%.
- Not all spectral lines follow the same behaviour. For instance, N V variability during cycle 1 is significantly higher than during cycle 2. The same occurs for O III] and Mg II.

The light curves of the main tracers are plotted in Figure 7. Cycle 1 flux variations are reminiscent of those observed in the high dispersion spectra of cycle 3 (see Paper II); at phase  $\sim 1$ , at the periapsis, there is a sudden increase in the flux that it is observed in N V, Si IV, C IV but also in singly ionized species such as C II or O I. During cycle 2, variations are softer and within the error bars for most tracers. Clearly, the observed trends change from one cycle to the next. It is noteworthy, that the semiforbidden transitions do not follow by the same trends than the permitted lines and their variability is not correlated.

---

<sup>2</sup>Let us denote as  $S_i$  each spectrum and  $N$  the number of spectra obtained in the cycle. The mean spectrum is computed as  $\langle S \rangle = (\sum_{i=1}^{i=N} S_i)/N$  and the standard deviation of the mean as,  $\sigma = ((\sum_{i=1}^{i=N} (S_i^2 - \langle S \rangle^2))/(N(N-1)))^{1/2}$

### 3.3. Flux-flux relations and accretion shock diagnostics

Radiation from an accretion shock has a markedly different spectral energy distribution than radiation from a cool star atmosphere. In cool stars, magnetic energy is transported from the stellar surface onto the atmosphere where it is dissipated into three main regions: the warm ( $T \sim 10^4$  K) chromosphere, the hot ( $T \geq 10^6$  K) corona and the transition region (TR) between them. The TR is a very thin layer (some  $10^4$  km thickness in the Sun) where the temperature increases by two orders of magnitude and it can only be observed at UV wavelengths. There are well characterized correlations between the flux radiated in the various spectral tracers of these regions; chromospheric (neutral and singly ionized species), TR (C III, Si III, Si IV, C IV, N V, He II...) and coronal spectral tracers (highly ionized species, O VI, X-ray flux...). These so-called flux-flux relations are used to model energy transport in cool stars and call for a universal mechanism operating in them (Ayres et al. 1995, Mihalas 1978).

Flux-flux relations have also been studied in TTSs (Huélamo et al. 1998, Johns-Krull et al. 2000, Yang et al. 2012, Gómez de Castro & Marcos-Arenal 2012, hereafter GdCMA). When compared with their main sequence analogues, it becomes evident that there is excess radiation from low ionization species (C II, Mg II, OI) with respect to the highly ionized ones (C IV, Si IV, He II). This indicates that radiation is released by a different mechanism than in cool stars. The most successful models propose that the excess gravitational energy of the accreting matter is released into heating at accretion shocks where the temperature reaches 0.3-1 MK, i.e., coronal-like temperatures, driving a photoionization cascade that results in the observed scalings (Calvet & Gullbring 1998, Gómez de Castro & Lamzin 1999).

AK Sco monitoring provides a unique chance to evaluate how these scalings behave during an accretion event and hence test the theoretical models. Of the many possible

flux-flux relations we should focus in four: C IV versus O I, C IV versus C II, C IV versus He II and Si III] versus C III]. To study AK Sco behaviour in the context of the TTSs properties, all observations of TTSs obtained with HST and STIS G140L and G230L gratings have been downloaded from the Hubble archive and the fluxes of the O I, C II, C IV, He II, Si III]<sub>1892</sub> and C III]<sub>1908</sub> lines have been determined.

The C IV versus OI flux-flux relation is optimal to evaluate the relative abundance between highly ionized and neutral species in the TTSs environment; it shows the largest deviation from the trend observed in main sequence stars (see GdCMA). Figure 8 shows that AK Sco falls in the TTSs trend and that from cycle 1 to cycle 2 moves along the trend with the largest fluxes being observed in cycle 2. Both cycles are neatly separated in the plot. Moreover, the intra-cycle variations are significantly smaller than the inter-cycle ones. Note that AK Sco fluxes are the sum of the contribution of the two components of the system. To evaluate the contribution from each component is not trivial since according to numerical simulations the accretion flow may be preferentially channeled in any of them (Paper I); splitting the flux in equal parts between the two components is equivalent to shifting by 0.3 dex the location of AK Sco in the diagram.

Cycles 1 and 2 are markedly different. During cycle 2, there are not significant variations in the line fluxes however, this is not the case in cycle 1; the OI flux increases by a 20% from the beginning to the end of the cycle while the C IV flux increases by a  $\pm 7\%$  in the same time lapse. The overall flux increase could be accounted by a decrease in the extinction but the markedly decrease of the C IV flux at the beginning of the cycle cannot be explained by an extinction effect.

The trends observed in the C IV-O I flux-flux diagram are reproduced in the C IV-C II flux-flux and the C IV-He II flux-flux diagrams (see, Figure 9 and 10, respectively). AK Sco observations are located on the regression line of the TTSs in the C IV-C II diagram

and they are slightly up in the C IV-He II diagram, similarly to what observed in the C IV-O I diagram.

The ratio  $\text{Si III]/C III]}$  is density sensitive and it is often used to measure the electron density of warm plasma in the atmosphere of late-type stars and TTSs (Brown et al. 1984, Gómez de Castro & Verdugo 2001, 2003). In AK Sco,  $\text{Si III]/C III]} \simeq 2$ , similar to what observed in the TTSs (see Figure 11), and indicates that the electron density of the emitting plasma is in the range  $10^9 \text{ cm}^{-3}$  to  $10^{11} \text{ cm}^{-3}$  depending on the precise plasma temperature (see Figure 4, in Gómez de Castro & Verdugo, 2001). The  $\text{Si III]/C III]}$  ratio does not vary significantly from cycle to cycle ( $2.2 \pm 0.6$  in cycle 1 and  $2.0 \pm 0.3$  in cycle 2) even though the line fluxes do vary. The first exposure in each cycle has very good SNR and it can be used as a pivot to measure variations during cycle. Again, a markedly different behavior is observed between cycle 1 and cycle 2. During cycle 2, no significant variations are observed ( $1\text{-}\sigma$  and  $2\text{-}\sigma$  confidence ellipse are displayed in the plot). However, in cycle 1 there is a significant variation between the first exposure (phase 0.9939) and that at phase 0.9993, when the lines ratio increases by a 37% and thus, the electron density of the plasma.

#### 4. Results from COS monitoring

The mean profiles of the main transitions are displayed in Figure 12; the profiles are very broad and centered at rest (the radial velocity of the system is  $1.3 \text{ km s}^{-1}$ ). The two spectroscopic components are not resolved in spite of their high relative velocity at periastron passage; from  $170$  and  $190 \text{ km s}^{-1}$  during the monitored phase interval (Alencar et al. 2003). The highest asymmetry is observed in the He II transition; as shown in Figure 13, after periastron passage, the line becomes significantly redshifted ( $95 \text{ km s}^{-1}$ ). This redshift cannot be caused by mass infall; though He II is a very sensitive tracer of accretion, He II observations of TTSs show that it is only slightly redshifted, if at all

(Gómez de Castro 2013). However,  $95 \text{ km s}^{-1}$  is the expected radial velocity of one of the two components of the system at periastris thus, the observed shift of the He II flux enhancement indicates that at periastron accretion is preferentially driven into one of the two components.

A similar trend is observed in the rest of the accretion tracers though blurred by the large broadening of the profiles. To visualize it better, we have computed the *excess* profiles obtained by subtracting the first observation (phase=0.9920 for G130M and phase=0.9930 for G160M) from the rest. In Figure 14, the excess profile is represented as a hyper-surface in phase and wavelength for the main lines. The increase of the red-wards shifted component flux from phase 1.0034 on is clearly noticeable in the Si IV, C V, N V and Si III lines. At the same time, the blue-wards shifted component becomes dimmer. This behavior is observed in all hot gas lines, regardless of the COS grating setting or detector segment from which the data were extracted. It is also in marked contrast to the COS observations of H<sub>2</sub>. The uncertainty of the COS wavelength solution is  $\approx 15 \text{ km s}^{-1}$  (Holland et al. 2014, *COS Instrument Handbook*), therefore we consider the systematic redshifts of the emission lines to be a real effect. The profiles of the *CIV excess* are also plotted in Figure 15. They show an increasing absorption in the blue edge of the line that it is caused by a progressive decrease of the flux in the blue-wards shifted part of the profile compared with the beginning of the periastron passage. One may naively think that this effect is caused by a decrease in the C IV flux (hence the accretion rate) from the companion ( $V_{rad} \in [-95, -85] \text{ km s}^{-1}$ ) however, the sharp edge at  $286 \text{ km s}^{-1}$  precludes this interpretation. There is also an H<sub>2</sub> emission line on the blue-wing of C IV 1548 (see Herczeg et al. 2002, France et al. 2014) however, variations in the H<sub>2</sub> could not caused the observed edge since the line is very narrow and H<sub>2</sub> variability is decoupled from the atomic species (see Paper II).

The light curve of the excess is displayed in Figure 16 for the main spectral lines. The

fastest rise is observed in He II; the excess rises by a factor of 4 in one hour. The C IV light curve is significantly softer (*excess* growth rate of 2.3 per hour). The maximum *excess* is observed from phase 1.01 on (3.26 hours after periapsis).

## 5. Accretion and cycle-to-cycle variations

The AK Sco binary system has a highly eccentric orbit, as a result when the system approaches periastron, the outer boundaries of the circumstellar disks (and the accretion streams passing by) get close enough one to each other to effectively lose the angular momentum, leading to an increase of the accretion rate. The predictions from numerical simulations for some sample cycles are shown in Figure 17; most often, the accretion flow is not evenly distributed between the two components of the system. In fact, there is a pronounced asymmetry in some cycles, see *i.e.* cycle 12 in Figure 17. Inter-cycle variations do not occur only in the total amount of the accretion rate but also on the details of the temporal distribution of the infall that shows in the light curves of the relevant spectral tracers.

The Hubble observations confirm these predictions:

- During cycle 1, there is a blueing of the near UV continuum and an increase of the line flux at phase 0.9982-0.9993 by  $\sim 10\%$ . The increase is pronounced in OI, C II, and Si IV and it is less prominent in saturated (Mg II, C IV) or weak (N V, He II) transitions. This evolution cannot be interpreted as an increase of the fraction of the stellar surface affected by the accretion shock; rather, the variations observed in the flux-flux diagrams call for a variation in the accretion rate and the electron density at the shock front. It is noteworthy that the Si III]/C III] ratio rises by a 37% from phase 0.992 to phase 0.9993 ([1] and [3] in Figure 11) corresponding to an increase of

the electron density by a factor of  $\sim 10$  for a fiducial temperature of 50,000 K. These observations are consistent with the theoretical prediction of enhanced mass-infall (accretion rate) at periastron.

- During cycle 2, the flux is higher but there are not significant variations during the monitored time lapse.
- During cycle 3, the behavior observed in cycle 1 seems to be reproduced. Moreover, the He II and CIV profiles show evidence of the accretion rate enhancement being channeled preferentially onto one of the two components of the system.

The UV radiation studied in this work is mainly produced at accretion shocks or very close to the stellar surface. Numerical calculations of the structure of accretion shocks in TTSs indicate that the C III], O III] and Si III] lines should have comparable intensities and that their ratios can be reliably used to derive the density, accretion infall velocity and hence, accretion rate on these stars (Gómez de Castro & Lamzin 1999). Though C III] and Si III] transitions could also be excited at the base of the jets (Gómez de Castro & Verdugo 2001), the profiles of these lines in AK Sco clearly indicate that any contamination by a possible jet is negligible (Gómez de Castro 2009), see also Sect. 6. The location of AK Sco in the Si III]/O III] versus Si III]/C III] diagram is displayed in Figure 18. There are not significant variations during the HST monitoring and, in all cases, the observations indicate that the emission is produced by low temperature (mild shock) and low density (low accretion rate) plasma. The electron density inferred is  $3 - 4 \times 10^{10} \text{ cm s}^{-3}$  in good agreement with the predictions from generic collisional plasma diagnosis.

The Si III]/O III] ratio varies from  $3.2 \pm 0.4$  in the first observation of cycle 1 (the one with the highest SNR) to  $2.6 \pm 0.3$  in the first observation of cycle 2; though this variation is marginal, it is suggestive of a change in the electron temperature from one

cycle to another. The Si III]/O III] ratio is temperature sensitive and in the accretion shock scenario, this variation is associated with a small change in the shock velocity; from  $200 \text{ km s}^{-1}$  to  $215 \text{ km s}^{-1}$ . Material in the shock front is heated by the release of the gravitational energy of the infalling material at the impact point; roughly  $T \simeq \mu v_{shock}^2 / 3k_B$ . The higher the shock velocity, the higher the electron temperature in the Si III], C III] lines formation region. Small variations in the end shock speed are to be expected since the angular momentum of the material in the innermost orbit might suffer slight variations due to the dynamics of the system (see Paper I).

## 6. Extended Ly $\alpha$ emission

Ly  $\alpha$ , Mg II and semiforbidden line radiation (C II], C III, Si III]) has been detected from jets and Herbig-Haro objects in TTSs (Coffey et al. 2004, López-Martínez & Gómez de Castro, 2015). We used the STIS  $52'' \times 0.2''$  slit to enable the possibility of a serendipitous detection of extended outflows from the AK Sco system. The STIS long-slit was oriented at position angles of  $28.5^\circ$  and  $36.6^\circ$  for visits 01 and 02, respectively. The objective here was to build up signal to look for the spectral signature of extended emission, and consequently all of the STIS G140L and G230L observations were coadded to maximize the chance of detection. The two dimensional spectra were aligned by fitting a Gaussian profile to the cross-dispersion profile of bright emission regions, C IV and the NUV continuum for G140L and G230L, respectively. The centroids of all of the individual exposures were then shifted to the spatial centroid of the initial exposure and the data were stacked. Centroid shifts were  $\leq 2$  pixels in all cases. Spatial profiles of several spectral regions of interest were then extracted from the coadded G140L and G230L spectral images.

Figure 19 shows the flux-normalized spatial profiles from the G140L (*top*) and G230L (*bottom*) observations. We created individual extractions of H I Ly $\alpha$ , C II, Si IV, the

1427 – 1520 Å region comprising H<sub>2</sub> emission and FUV continuum, C IV, and O III] from the G140L spectra. Mg II, an adjacent continuum region to Mg II, and two continuum regions dominated by Balmer continuum and stellar photosphere (2000 – 2620 Å and 2900 – 3040 Å) were extracted from the combined G230L observations. The Mg II profile is indistinguishable from the adjacent continua. The FUV emission lines (except possibly Ly $\alpha$ ) are also unresolved, with lines at shorter wavelengths displaying progressively broader profiles at flux levels  $\lesssim 2$  % of the peak. These are likely the result of the extended short-wavelength point spread function of the *HST* optical telescope assembly, owing primarily to mid-frequency errors related to the final quality of the telescope polish. The Ly $\alpha$  profile displays both a 1-pixel offset from the main FUV peak and evidence for spatial extension. We caution the reader that these profiles are extracted across the bright geocoronal Ly $\alpha$  emission line – the dotted line profile in Figure 5, *top*, shows the Ly $\alpha$  profile prior to airglow subtraction and the solid circles are the profile following the subtraction of a constant geocoronal airglow component, the average of 100 pixels centered approximately 4.3'' in the “+*y*” direction on the STIS FUV MAMA. Taking the nominal 103 pc distance (van Leeuwen 2007) and 68°inclination angle (Alencar et al. 2003) for AK Sco, > 90 % of the FUV line flux is located within  $\pm 9.3$  AU of the center of mass of the system, with > 90 % of the NUV flux originating within  $\pm 7.4$  AU from the center of mass. Our conclusion is that there is tentative evidence that AK Sco displays extended Ly $\alpha$  emission (subject to large uncertainties in the airglow subtraction), but that all of the other emissions originate within  $\approx \pm 10$  AU of the center of mass.

## 7. Light curve analysis: search for low frequency modes

In a previous work (Paper I), we reported the detection of an Ultra Low Frequency (ULF) oscillation in the UV light-curve from AK Sco using the Optical Monitor (OM)

instrument on-board the XMM-Newton. The ULF oscillation was excited close to the periastron passage, lasting only for few oscillations at the rise of the UV light curve. It had a period of  $790^{+200}_{-150}$  s and was detected with filter UVM2 (spectral range 2000 Å - 2700 Å). This bulk radiation may be produced in several distinct regions of the TTSs environment (chromosphere, accretion shock, photoionized gas in the inner disk...) making difficult the identification of the source. The spectral lines detected with COS cover a broad range of densities and temperatures hence the analysis of their light curves has the potential of enabling the identification of the source.

For this analysis, the COS event lists datasets have been used instead of the 1-D extracted spectra (.x1d files). The light-curve generation reads the segments A and B from FUV datafiles following the steps taken by the light-curve COS package from Ely et al. (2015). These light-curves were later on processed for computing the Lomb-Scargle Periodograms (Lomb 1976, Scargle 1982), using the standard astropy package. This method performs well with unevenly spaced data, as is our case. The Lomb-Scargle method essentially fits a sinusoidal model to the data at each frequency, with a larger power assigned to a given frequency reflecting a better fit. The selected normalization uses the residuals of the data around the constant reference model, leading to the resulting power  $P$  to be a dimensionless quantity between 0 and 1.

When using a Lomb-Scargle Periodogram and deciding whether a signal contains a periodic component, an important consideration is the significance of the peaks. In a Bayesian view, the Lomb-Scargle periodogram is the optimal statistic for detecting a stationary sinusoidal signal in the presence of Gaussian noise. Hence, this significance is usually expressed in terms of a false alarm probability (fap), which encodes the probability of measuring a peak of a given height (or higher) conditioned on the assumption that the data consists of Gaussian noise with no periodic component. A fap level of, let us say 1%

means that, under the assumption that there is no periodic signal in the data, we will observe a peak reaching such level high or higher only 1% of the time.

The COS monitoring of the periastron passage lasted about 9hrs. The Figure 20 shows the periodograms corresponding to the light-curves (see Paper II). The upper panel corresponds to the G130M data, and the bottom panel to the G160M data. The periodograms are built up to a maximum period of 2.0hrs. The peaks around the rightmost vertical line correspond to the detection of the HST orbital period of around 1.6hrs. The grey area shows the ULF interval as reported in (Gomez de Castro 2013). The periodogram panel also plots the horizontal lines corresponding to the required peak height to attain a false alarm probability (fap) of 10%, 5% and 1%.

In addition to the peaks linked to the HST orbital period, we observe other high peaks. The Lomb-Scargle periodograms detect all periodicities found in the data, including those periods corresponding to the observational sampling period and its  $1/n$  multiples. That is, they will also reflect combinations of the duration of exposures and separations between them.

In order to distinguish any real ULF periodicity from those aliased multiples, we have overlaid in the figure the periodograms resulting from fixing the real signal to an arbitrary value of 1. In this way, the pattern of the resulting peaks will exclusively correspond to the observational sampling.

The region where the ULF is suspected to be present is between 0.15 and 0.4hrs. Here, all the peaks are grouped and mimic those found at larger periods, which indicate they are alias from main frequencies. Unfortunately, the typical G160M exposure duration is around 0.22, and these peaks likely come from this sampling duration close to the searched ULF period. The results with G130M data are very similar. Fixing again the counts to an arbitrary unit value, we get the same pattern of peaks resulting from the observational

sampling. Finally, when computing the periodograms corresponding to the light-curves selecting certain wavelengths, such as C IV, Si IV (Hot species) and C II (warm species), the results are again comparable. Any periodicity within the ULF region may still exist, but with a really high fap, not distinguishable from noise. Outside the ULF region, one may search for other periodicities. But, in a similar manner, all the peaks with low fap are linked to the observing windows, and a clean up process of the sampling frequencies does not improve the results.

As an alternative, we can compute the periodograms just using individual exposures. The signal will be weaker and the fap levels may decrease, but the main sampling multiples will not be present. This analysis is seen in Figure 21. The upper panel shows the results coming from the G130M single exposures. We do not detect any periodicity in the ULF area. The G130M exposure labeled as ‘isq’ presents a peak around a period of 0.17hrs, but the corresponding fap is very high, around 83%, indicating that this could be produced by noise. The G160M analysis also presents peaks with a very high fap. However, as the G160M exposures were taken in consecutive pairs, this analysis uses longer duration light-curves. The results can be seen in the bottom panel of Figure 21. The pair labeled ‘jeq-jgq’ presents a peak around 0.25hrs, with a fap of %24. One may think this peak could be an alias of the double exposure duration. But, notably, such a peak is not present in any of the remaining curves. Hence, we may have a (faint) indication that the ULF was present at least during one of the exposures.

## 8. Summary and Conclusions

The observations provided by the dedicated Hubble’s monitoring of AK Sco have enabled for the first time to track the variability of a pre-main sequence binary with a degree of detail similar to that of the UV observations of interacting binaries. Much of

the observed behaviour was already predicted by numerical simulations (Paper I) but this campaign has provided the highly needed experimental evidence of the erratic cycle-to-cycle variations. Also the radiative output from accretion has been accurately measured rendering fundamental data for accretion shocks calculations.

Two other PMS interacting binaries had previously been monitored with Hubble namely, UZ Tau E and DQ Tau (Ardila et al 2015) but the phase coverage had significantly poorer temporal resolution and this is fundamental issue since, as shown in this work, the dynamics of these systems is very complex. Moreover, the gravitational piston effect of the passage by the periastron is less significant in them making more difficult the precise timing of the accretion events. DQ Tau, the system most similar to AK Sco, is composed of two equal mass stars with mass  $0.5 M_{\odot}$ , in a orbit less eccentric than AK Sco's one and with larger semi-major axis (Mathieu et al. 1997). The mass ratio of the components in UZ Tau E is 0.289 (Prato et al. 2003) thus mass infall is preferentially channelled in the primary and the effect is less significant.

AK Sco was monitored for two consecutive cycles in low dispersion (high sensitivity) with STIS and a third one with COS providing good time and kinematical resolution at the cost of a lower SNR in the flux. STIS data analysis revealed the enhancement of the accretion rate during the first periastron passage, supported by:

- Blueing of the 1640-3100 NUV continuum between 0.9982 and 0.9993 phases, in the middle of the cycle.
- Sudden increase in the flux of important accretion tracers, such as the NV, Si IV and C IV lines, and also in neutral singly ionized species such as O I and C II.
- Variations in the Si III]/C III] flux-flux diagrams, revealing variations in the electron density by an order of magnitude during the periastron passage.

This behavior is reproduced as well in the third cycle, in agreement with the previous analysis showed in Gómez de Castro et al. (2016). Moreover, the high resolution of COS make possible to recognize an increase in the red-wards shifted component in important accretion tracers (He II and C IV), while the blue-wards shifted component of these lines decreases, pointing out that accretion is preferentially driven into one of the two components of the system. These intra-cycle variations are in concordance with the results given in Paper I through the XMM-Newton monitoring of the AK Sco system, where the enhanced of the UV and X-ray flux in the binary was suggested to be produced by an accretion outburst.

Cycle-to-cycle variations have been measured as well, where the most remarkable feature is the notably increase in the total UV radiation of the system from cycle 1 to cycle 2. Moreover, between the two first cycles, the Si III]/O III] temperature-dependent ratio reveals a marginal variation of the plasma temperature, that could be translated into a small change in the shock velocity from 200 km/s to 215 km/s.

Despite the measured enhancement of the UV radiation in cycle 2, the absent of significant variations in the flux of spectral lines and in the flux-flux relations during this cycle reveals no hints about the accretion rate enhancement, in discordance with the other two cycles.

Beside accretion processes in the AK Sco system, the presence of extended emission due the presence of jets has been addressed in this study. Spatial cross-dispersion profiles of STIS data allowed us to identify hints of a diffused envelope around the AK Sco binary radiating in Ly $\alpha$ .

Finally, inspired by the detection of ultra-low frequency oscillations in AK Sco (Paper I), we analyzed the presence of these low-frequency modes in the light-curve of the binary,

however, the analysis of the UV light curve from COS data only shows a minor indication that the ULF may be present in the region where the C IV line is produced. This result requires further confirmation with a dedicated campaign monitoring AK Sco only with COS/G160M.

This work has been partly funded by the Ministerio de Economía y Competitividad of Spain through grant ESP-2017 -87813-R. The data presented here were obtained through *HST* Guest Observing program 13372.

*Facilities:* HST (COS), HST (STIS).

### A. The ultraviolet spectrum of F stars

For the processing and modelling of the UV continuum of AK Sco, and its variability, it is important to compare the UV spectrum of AK Sco with that of F-type main sequence stars. For this purpose, we have searched the archive of the International Ultraviolet Explorer (IUE) mission for observations of F stars (IUE object class 41). 924 observations were obtained of stars either in the 2000-3200 Å range (cameras LWP or LWR) or in the 1200-2000 Å range (camera SWP). We submitted the target list output from the IUE archive to the Centre of Données Stellaires de Strassbourg (program SIMBAD) for the sources cross-identification. We found that about 30% of the observations corresponded to RS Canis Venaticorum systems and spectroscopic binaries. Only single stars with well known spectral types were selected and from those, only stars with high SNR and non-saturated spectra in the 1200-3200 Å (see Table A1).

The spectra are shown in Fig. A1. Three windows can be readily identified: W1(1640-2400 Å), W2(2400-2775 Å) and W3(2775-3100 Å). W1 contains the UV bump and the high energy tail of the spectrum; it is most prominent in early types. W2 is dominated

by the Fe II multiplets (2,3,32-36,62,63,363). Flux in W3 increases for the late spectral types as the W1 flux decreases. This permits using the rates between the integrated fluxes in these windows,  $F(W1)/F(W2)$  and  $F(W2)/F(W3)$ , as spectral subtype (or effective temperature) indicators.

## REFERENCES

- Alencar, S. H. P., Melo, C. H. F., Dullemond, C. P., et al. 2003, *A&A*, 409, 1037
- Alexander, R. D., Clarke, C. J., & Pringle, J. E. 2004, *MNRAS*, 354, 71
- Alexander, R., Pascucci, I., Andrews, S., et al. 2014, *Protostars and Planets VI*, 475
- Andersen, J., Lindgren, H., Hazen, M. L., et al. 1989, *A&A*, 219, 142
- Artymowicz, P. & Lubow, S. H. 1994, *ApJ*, 421, 651
- Ayres, T. R., Fleming, T. A., Simon, T., et al., 1995, *ApJS*, 96, 223
- Bate, M. R. & Bonnell, I. A. 1997, *MNRAS*, 285, 33
- Brown, A. de M. Ferraz, M. C. and Jordan, C., 1984, *Royal Astronomical Society*, 207, 831
- Calvet, N. & Gullbring, E. 1998, *ApJ*, 509, 802
- Clarke, C. 2011, *Physical Processes in Circumstellar Disks around Young Stars*, 355
- de Val-Borro, M., Gahm, G. F., Stempels, H. C., et al. 2011, *MNRAS*, 413, 2679
- Ely, J., Bourque, M., Debes, J., et al. 2015, *IAU General Assembly*
- Ercolano, B., Clarke, C. J., & Drake, J. J. 2009, *ApJ*, 699, 1639
- Fitzpatrick, E. L. & Massa, D. 2007, *ApJ*, 663, 320
- Font, A. S., McCarthy, I. G., Johnstone, D., et al. 2004, *ApJ*, 607, 890
- Gómez de Castro, A.I. & Lamzin, S., 1999, *Monthly Notices of the R.A.S.*, 304, L41
- Gómez de Castro, A. I., & Verdugo, E. 2001, *ApJ*, 548, 976
- Gómez de Castro, A. I., & Verdugo, E. 2003, *ApJ*, 597, 443

- Gómez de Castro, A. I. 2009, ApJ, 698, L108
- Gómez de Castro, A.I., Marcos-Arenal, P., 2012, ApJ, 749, 190
- Gómez de Castro, A. I. 2013, Planets, Stars and Stellar Systems. Volume 4: Stellar Structure and Evolution, 279
- Gómez de Castro, A. I., López-Santiago, J., Talavera, A., et al. 2013, ApJ, 766, 62 (Paper I)
- Gomez de, C. A. I., Lopez-Santiago, J., & Talavera, A. 2013, MNRAS, 429, L1
- Gómez de Castro, A. I. 2013, ApJ, 775, 131
- Gomez de Castro, A. I. & Marcos-Arenal, P. 2015, XI Multifrequency Behaviour of High Energy Cosmic Sources Workshop (MULTIF15), 19
- Gómez de Castro, A. I., Loyd, R. O. P., France, K., et al. 2016, ApJ, 818, L17 (Paper II)
- Gontcharov, G. A. 2006, Astronomical and Astrophysical Transactions, 25, 145
- Gorti, U. & Hollenbach, D. 2009, ApJ, 690, 1539
- Guenther, E. W., Esposito, M., Mundt, R., et al. 2007, A&A, 467, 1147
- Hanawa, T., Ochi, Y., & Ando, K. 2010, ApJ, 708, 485
- Holland, S. T., et al. 2014, Cosmic Origins Spectrograph Instrument Handbook, Version 6.0 (Baltimore: STScI)
- Hollenbach, D., Johnstone, D., Lizano, S., et al. 1994, ApJ, 428, 654
- Huélamo, N., Gómez de Castro, A. I., & Franqueira, M. 1998, Ultraviolet Astrophysics Beyond the IUE Final Archive, 413, 121
- Johns-Krull, C. M., Valenti, J. A., & Linsky, J. L. 2000, ApJ, 539, 815

- Lomb, N. R. 1976, *Ap&SS*, 39, 447
- Melo, C. H. F., Covino, E., Alcalá, J. M., et al. 2001, *A&A*, 378, 898
- Mihalas, D. 1978, San Francisco: W.H. Freeman, 1978
- Shi, J.-M., Krolik, J. H., Lubow, S. H., et al. 2012, *ApJ*, 749, 118
- Scargle, J. D. 1982, *ApJ*, 263, 835
- Schneider, G., Grady, C. A., Hines, D. C., et al. 2014, *AJ*, 148, 59
- van Leeuwen, F. 2007, *A&A*, 474, 653
- Yang, H., Herczeg, G. J., Linsky, J. L., et al. 2012, *ApJ*, 744, 121

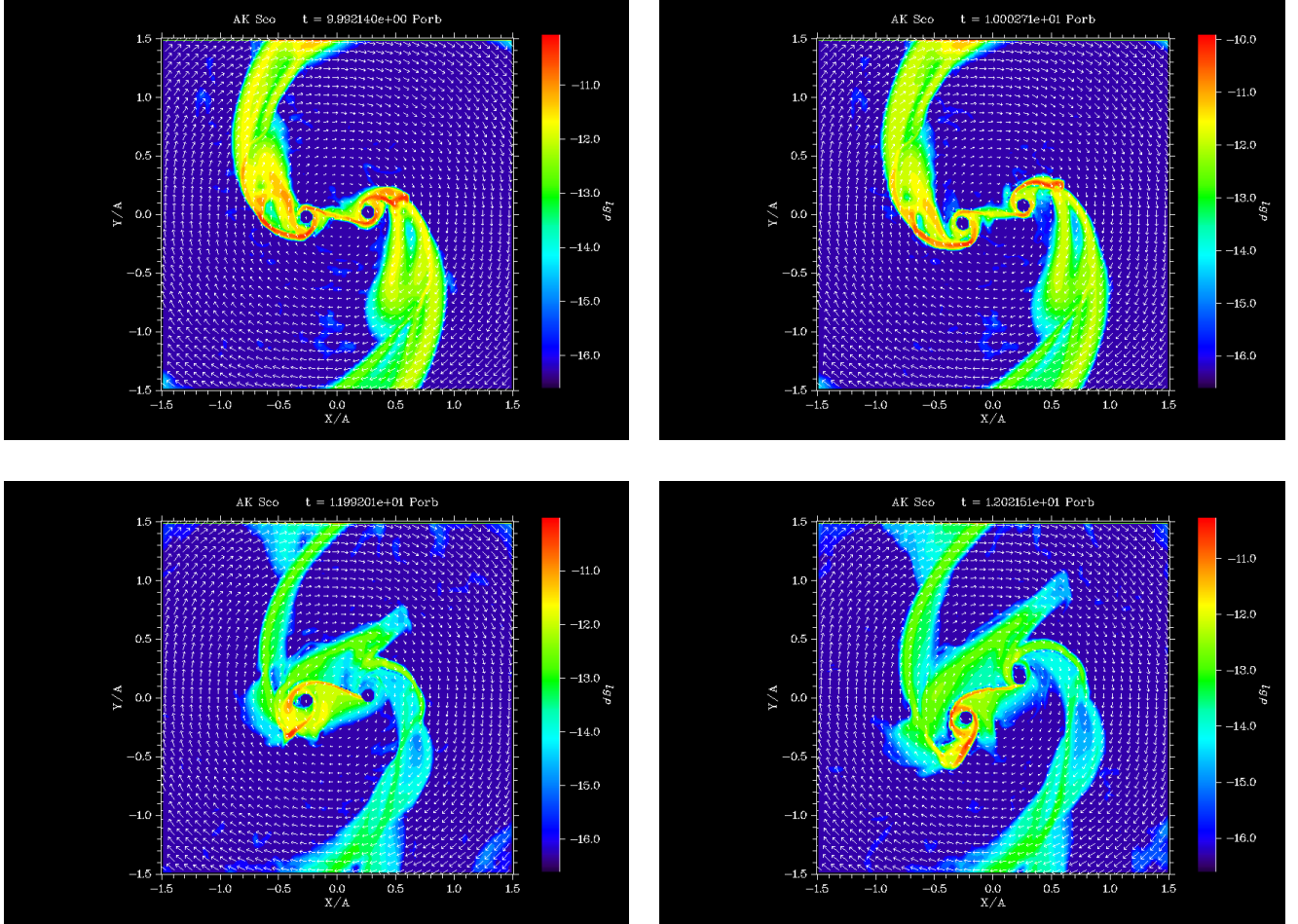


Fig. 1.— Theoretical predictions of the evolution of the density distribution in the inner gap during the periastron passage for any two cycle; cycle 1 top panels, cycle 2 bottom panels. Note that the mass infall is channelled differently from cycle to cycle making the physical configuration not exactly repeatable. Left panels correspond to phase 0.992 and right panels to phase 1.02 (approximately the phase coverage of the HST monitoring). Each frame represents a physical size of  $3 \times 3$  times the semimajor axis of the orbit ( $0.23\text{AU} \times 0.23\text{AU}$ ). In the figure, AK Sco system is displayed from a pole-on view (i.e.  $i = 0^\circ$ ) for better visualization but the inclination of the system is  $65^\circ - 70^\circ$  (see Table 1).

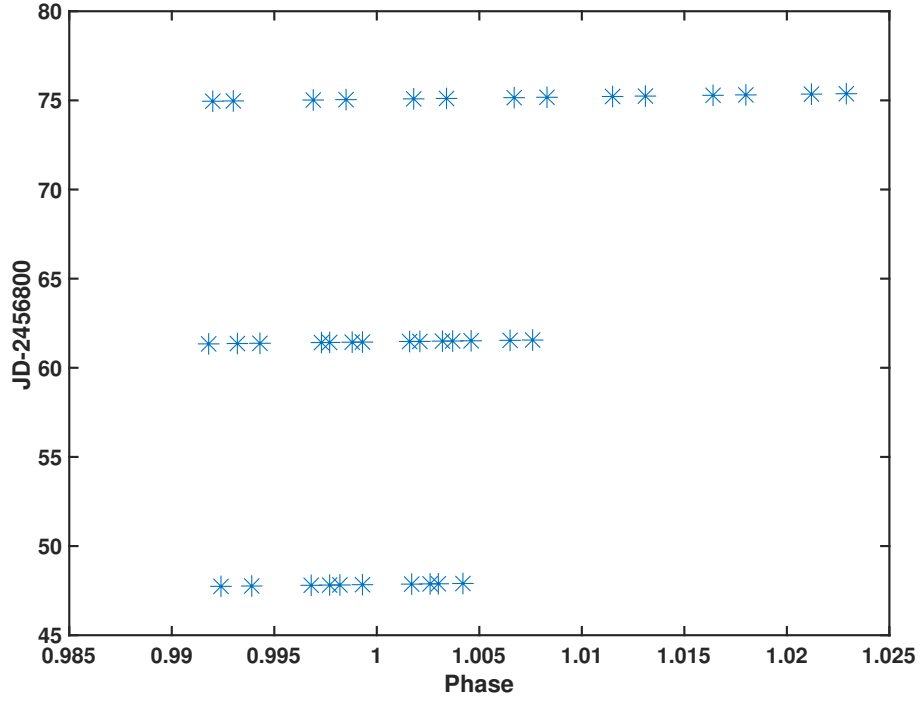


Fig. 2.— The main characteristics of the monitoring program are outlined. AK Sco was tracked during three consecutive periastron passages. During the first two passages it was observed with STIS, using grating G140L (1140 Å- 1730 Å) and G240L (1568 Å- 3184 Å). COS was used for the last passage covering the 1160 Å- 1453 Å range and then, the 1402 Å- 1762 Å range. All observations were carried in photon counting mode.

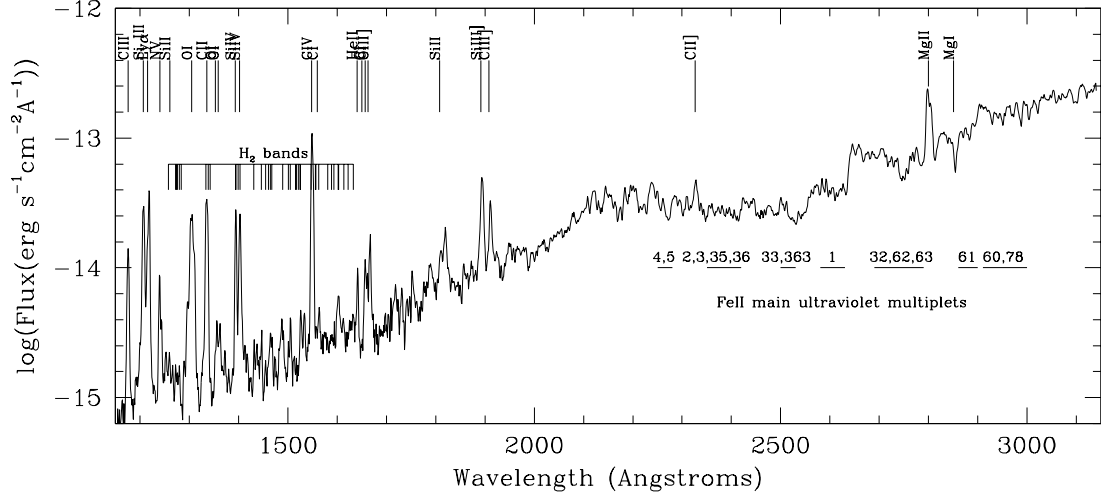


Fig. 3.— Average spectrum of AK Sco from STIS observations. The main spectral features are marked.

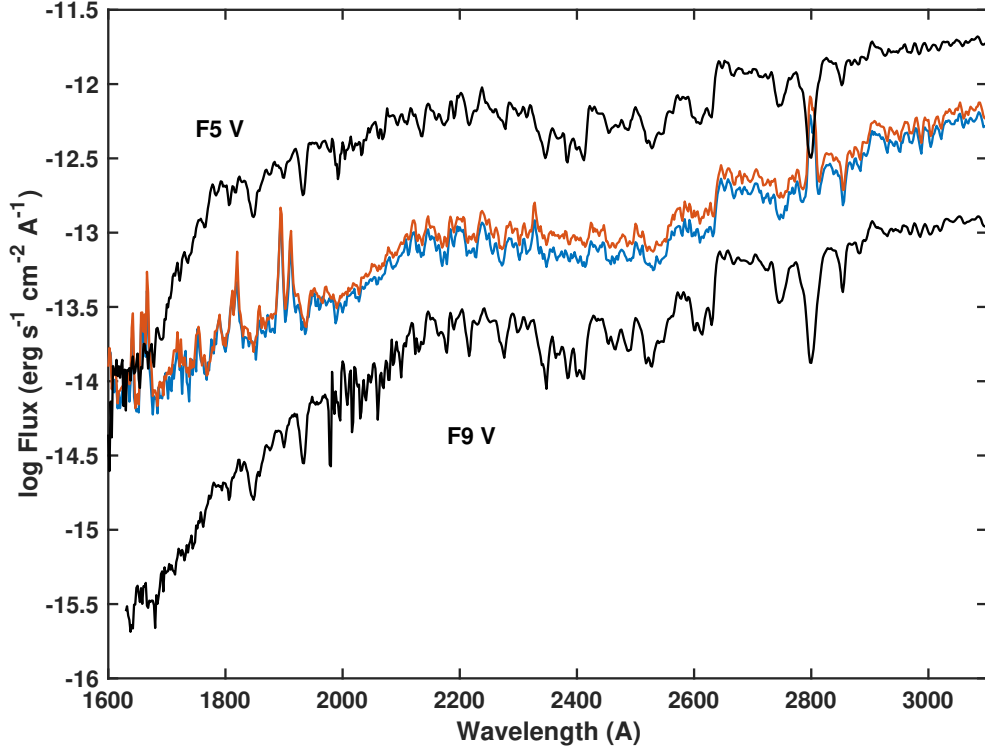


Fig. 4.— Average spectrum of AK Sco during cycle 1 (blue) and cycle 2 (red), STIS observations. The UV spectrum of the F5 V star, HD 139664 and the F9 V star, HD 22879 are plotted (grey) for comparison; they have been offset by -1.2 dex and -2.5 dex respectively, for the plot.

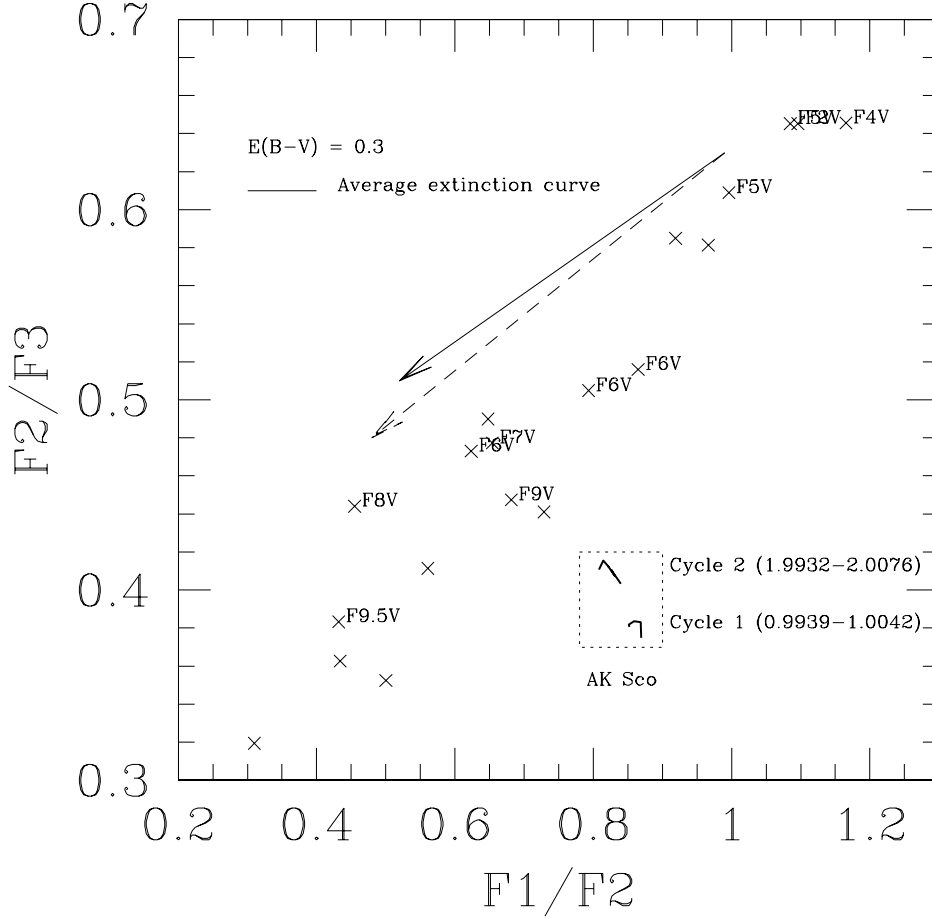


Fig. 5.— Variation of the location of AK Sco in the  $R1 = F1/F2$  and  $R2 = F2/F3$  space during the monitorings run with HST/STIS. The location of main sequence F stars is indicated as well as the extinction arrow (solid) for the average ISM extinction law (Fitzpatrick & Massa, 2007) and the modified extinction law ( $R = 4.3$ ) found by Manset et al. (2004) to be representative of the circumstellar environment in AK Sco (dashed arrow). Notice that extinction runs roughly parallel to the spectral types. AK Sco spectrum has not been dereddened for the plot but its location close to late spectral types (F7V-F9V) instead of F5 cannot be fully ascribed to extinction; AK Sco extinction  $A_V = 0.5$  or  $E(B - V) = 0.12$  (Manset et al. 2005).

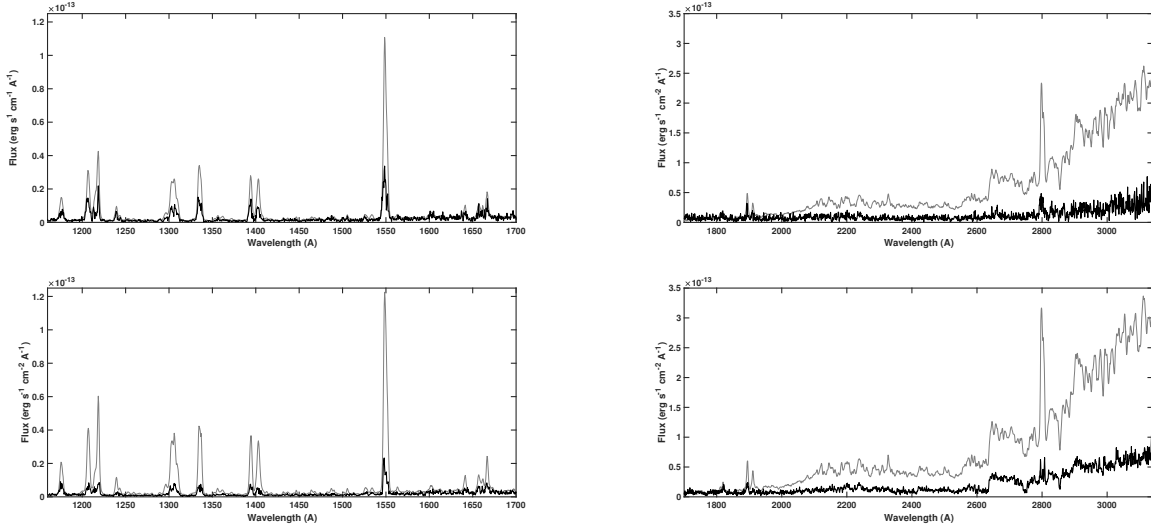


Fig. 6.— Spectral variability during cycles 1 (top) and 2 (bottom). The average spectra is displayed in grey and the dispersion around the mean in thick black; the dispersion has been multiplied by 10 for the plot (in all the panels).

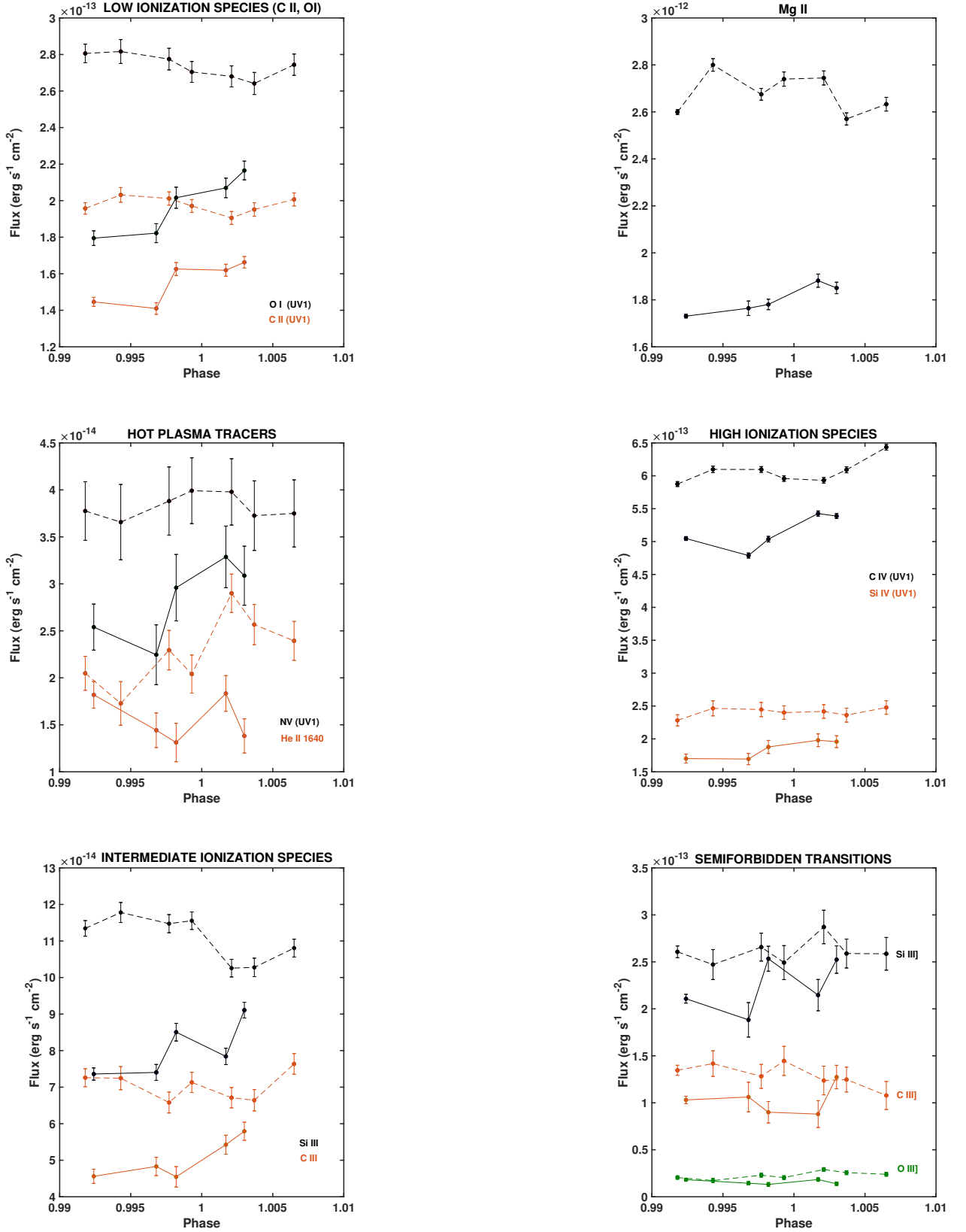


Fig. 7.— Light curves of the main spectral lines during cycles 1 (solid) and 2 (dashed); 1- $\sigma$  error bars are indicated.

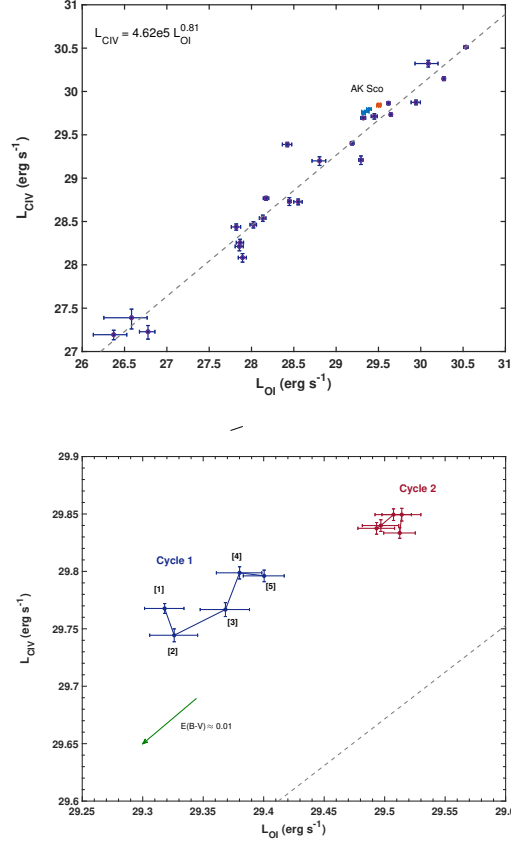


Fig. 8.— C IV - OI flux-flux diagram. Top, diagram for all the T Tauri stars observed with Hubble with the same configuration (STIS/G140L). AK Sco observations are plotted in blue (cycle 1) and red (cycle 2). The regression line is indicated. Bottom, zoom on the location of AK Sco observations. The order of the observations in cycle 1 is marked as [1], [2].... .  $1-\sigma$  error bars are plotted.

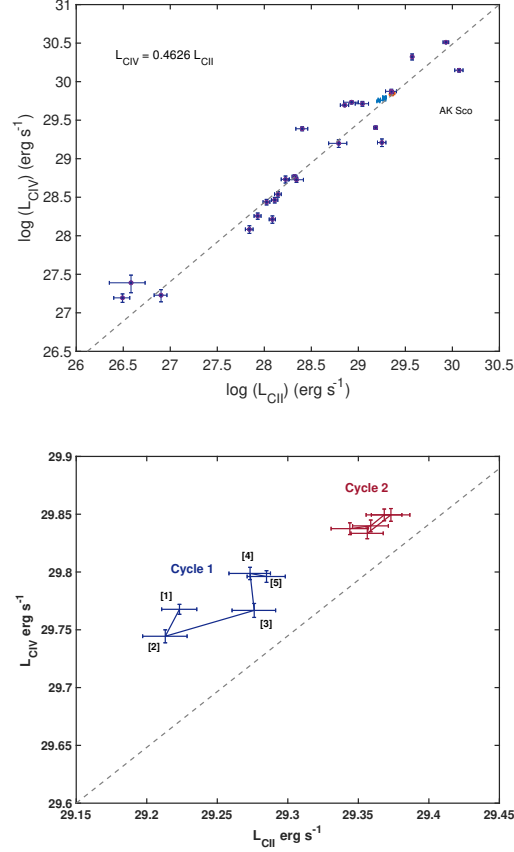


Fig. 9.— C IV - C II flux-flux diagram. Top, diagram for all the T Tauri stars observed with Hubble with the same configuration (STIS/G140L). AK Sco observations are plotted in blue (cycle 1) and red (cycle 2). The regression line is indicated. Bottom, zoom on the location of AK Sco observations. The order of the observations in cycle 1 is marked as [1], [2].... 1- $\sigma$  error bars are plotted.

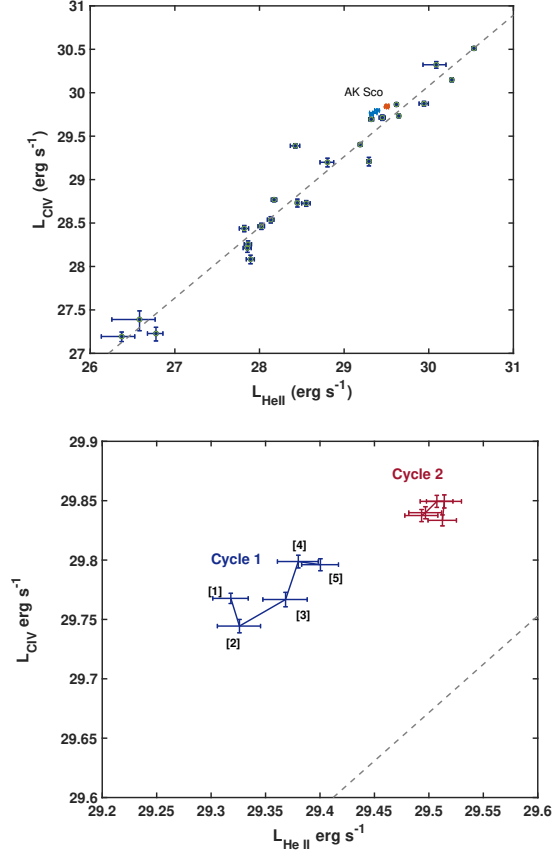


Fig. 10.— C IV - He II flux-flux diagram. Top, diagram for all the T Tauri stars observed with Hubble with the same configuration (STIS/G140L). AK Sco observations are plotted in blue (cycle 1) and red (cycle 2). The regression line is indicated. Bottom, zoom on the location of AK Sco observations. The order of the observations in cycle 1 is marked as [1], [2]....  $1\text{-}\sigma$  error bars are plotted.

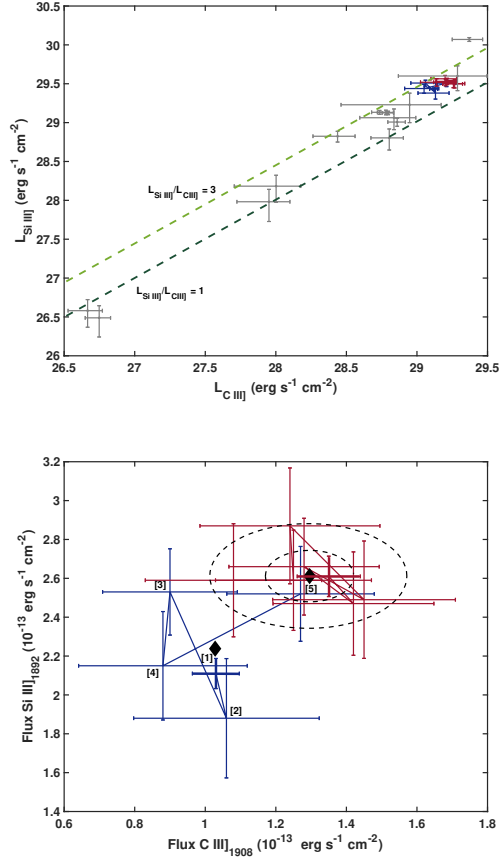


Fig. 11.— Si III] - C III] flux-flux diagram. Top, diagram for all the T Tauri stars observed with Hubble with the same configuration (STIS/G140L). AK Sco observations are plotted in blue (cycle 1) and red (cycle 2). The lines corresponding to Si III]/C III]=1 and 3 are marked with dashed lines. This ratio is sensitive to the electron temperature; for  $T_e \simeq 5 \times 10^4$  K this range corresponds to a variation in electron density from  $10^{10} \text{ cm}^{-3}$  to  $10^{11} \text{ cm}^{-3}$ . Bottom, zoom on the location of AK Sco observations. The black diamonds mark the location of the average values during cycle 1 and 2. The 1- $\sigma$  and 2- $\sigma$  confidence ellipse for cycle 2 observations is marked with dashed lines. The order of the observations in cycle 1 is marked as [1], [2].... 1- $\sigma$  error bars are indicated for all observations. Note the significantly better SNR of the first observation in each cycle (bold error bars).

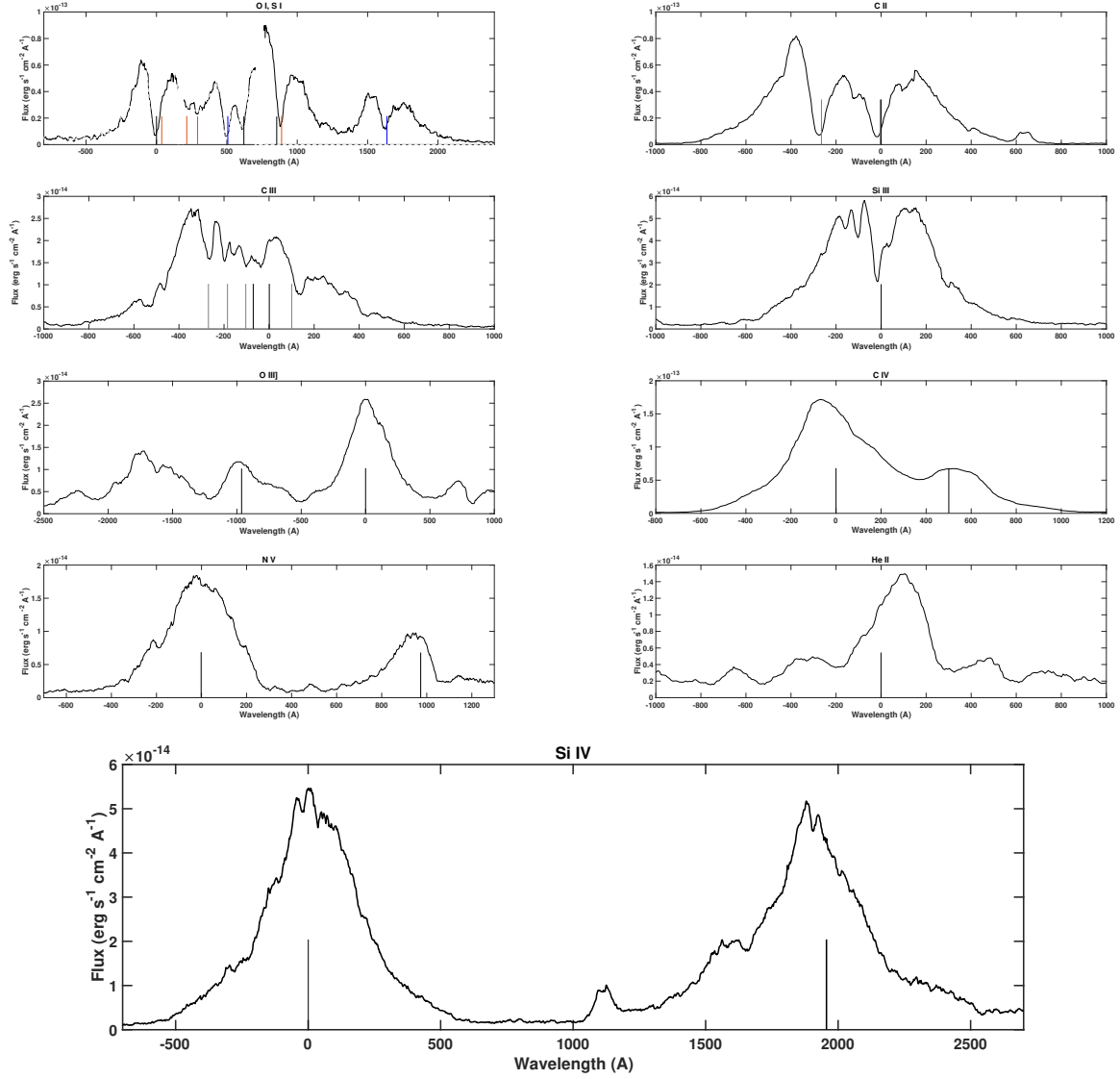


Fig. 12.— Mean profiles of the main atomic transitions during the COS monitoring. The rest wavelengths of the atomic transitions are marked for reference; in the OI, SI panel these references are colour coded (black OI, orange SI and blue Si II).

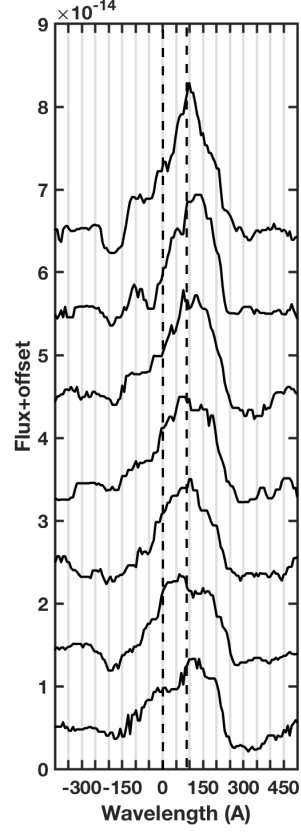


Fig. 13.— Variation of the He II profile with the phase; phase increases from bottom to top. The dashed lines mark the radial velocity of AK Sco ( $-1.3$  km/s) and radial velocity  $95$  km/s corresponding to the orbital solution at phase 0 for one of the two components of the binary (Alencar et al. 2003).

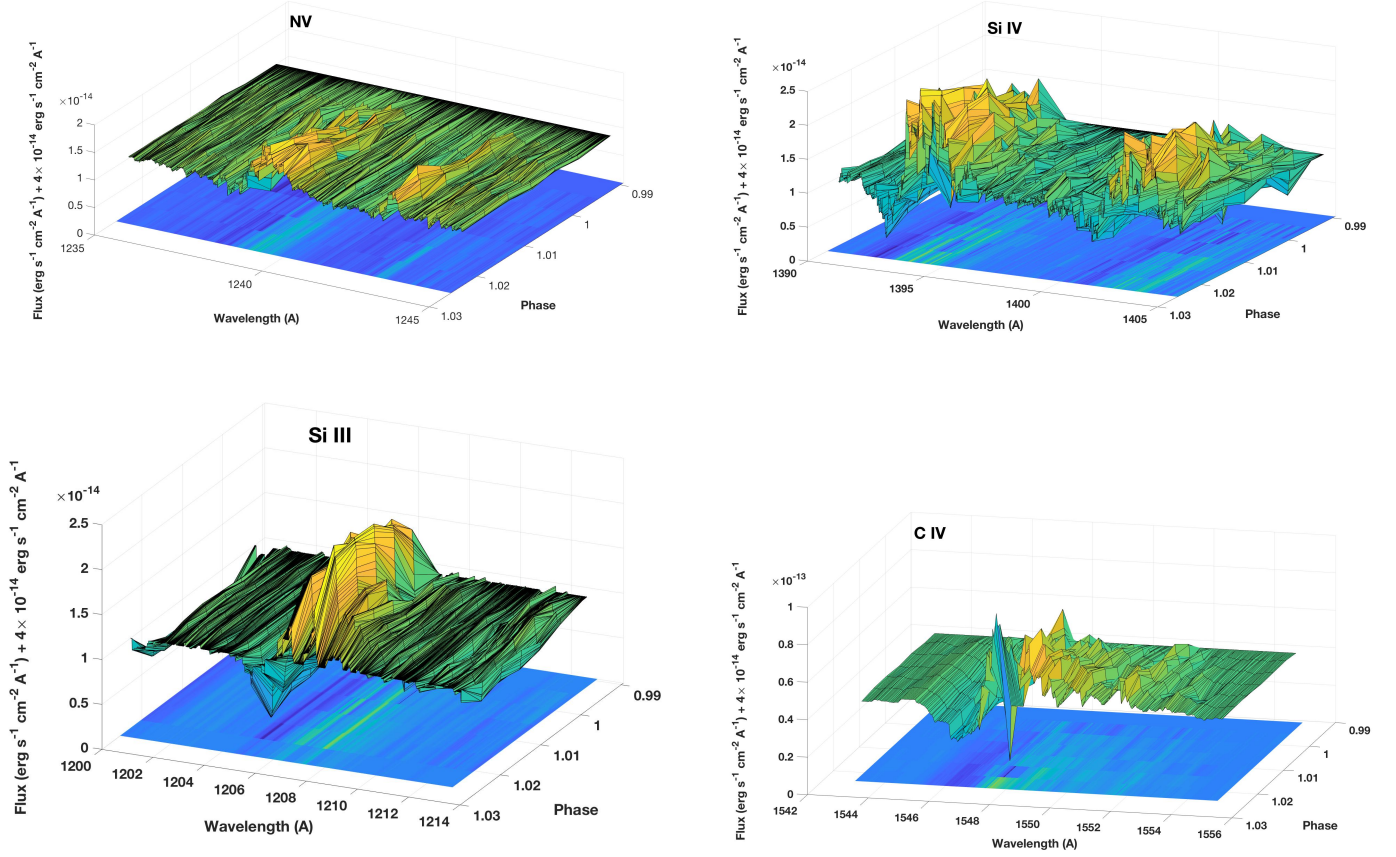


Fig. 14.— Variability of the N V, Si IV, Si III and C IV profiles during COS monitoring. The evolution of the profile during periastron passage is shown by subtracting the profile at phase 0.9920 from the rest and making a 3-D plot. Note that just after periastron, the flux is enhanced. Also a weak absorption develops at high blue-wards shifted velocities (250 km/s). From top to bottom and from left to right: N V, Si IV, Si III and C IV.

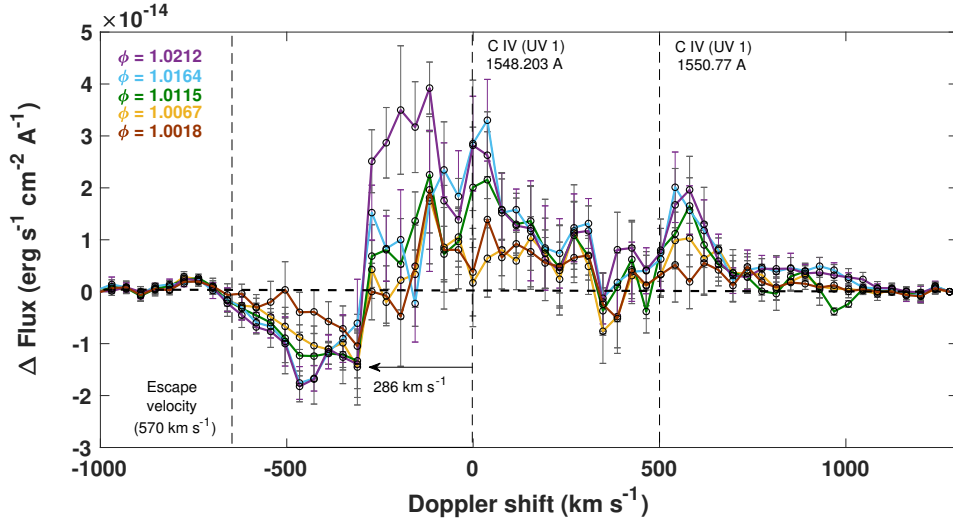


Fig. 15.— Variation of the CIV profile during cycle 3. The excess CIV emission with respect to the first two observations in cycle 3 is plotted, with  $1\sigma$  error bars. The rest wavelengths of the doublet lines, at the radial velocity of the AK Sco binary system are marked. The radial component of the orbital velocity of each component is  $\pm 90 \text{ km s}^{-1}$  with respect to the systemic velocity. The peak of the CIV,  $1550.77 \text{ \AA}$  line, is redshifted by this amount, similarly to what observed in the He II line (see Figure 14).

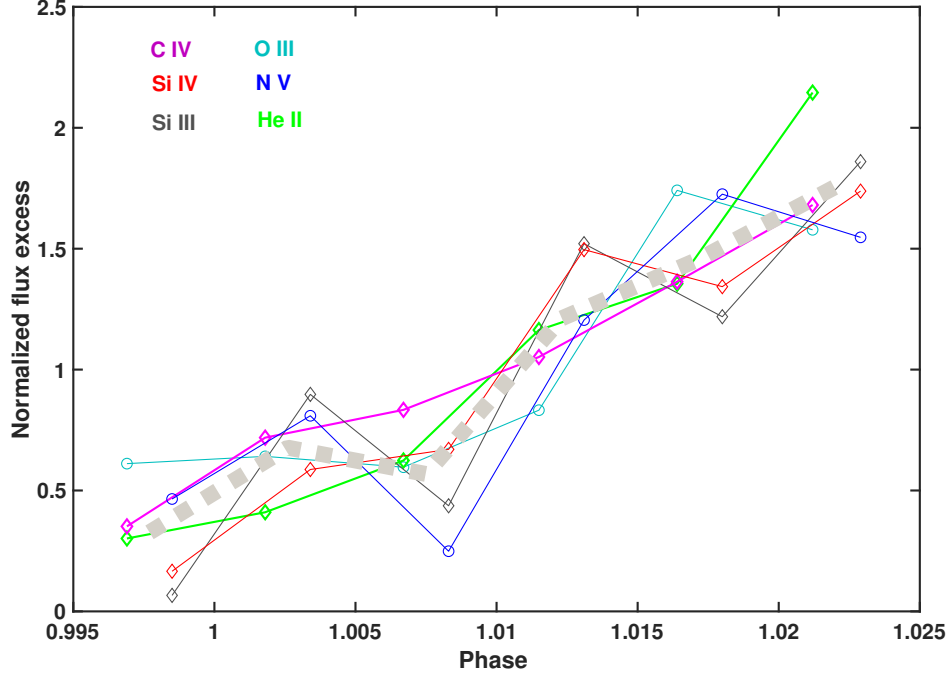


Fig. 16.— Variation of the flux excess during periastron passage for the main spectral tracers. The curves have been normalized to the average excess with values of  $6.49 \times 10^{-13} \text{ erg s}^{-1} \text{ cm}^{-2}$ ,  $1.079 \times 10^{-12} \text{ erg s}^{-1} \text{ cm}^{-2}$ ,  $1.311 \times 10^{-12} \text{ erg s}^{-1} \text{ cm}^{-2}$ ,  $1.03 \times 10^{-13} \text{ erg s}^{-1} \text{ cm}^{-2}$ ,  $2.32 \times 10^{-13} \text{ erg s}^{-1} \text{ cm}^{-2}$  and  $0.98 \times 10^{-13} \text{ erg s}^{-1} \text{ cm}^{-2}$  for Si III, Si IV, C IV, He II, O III and N V lines, respectively. The average light curve is marked with a thick dashed line.

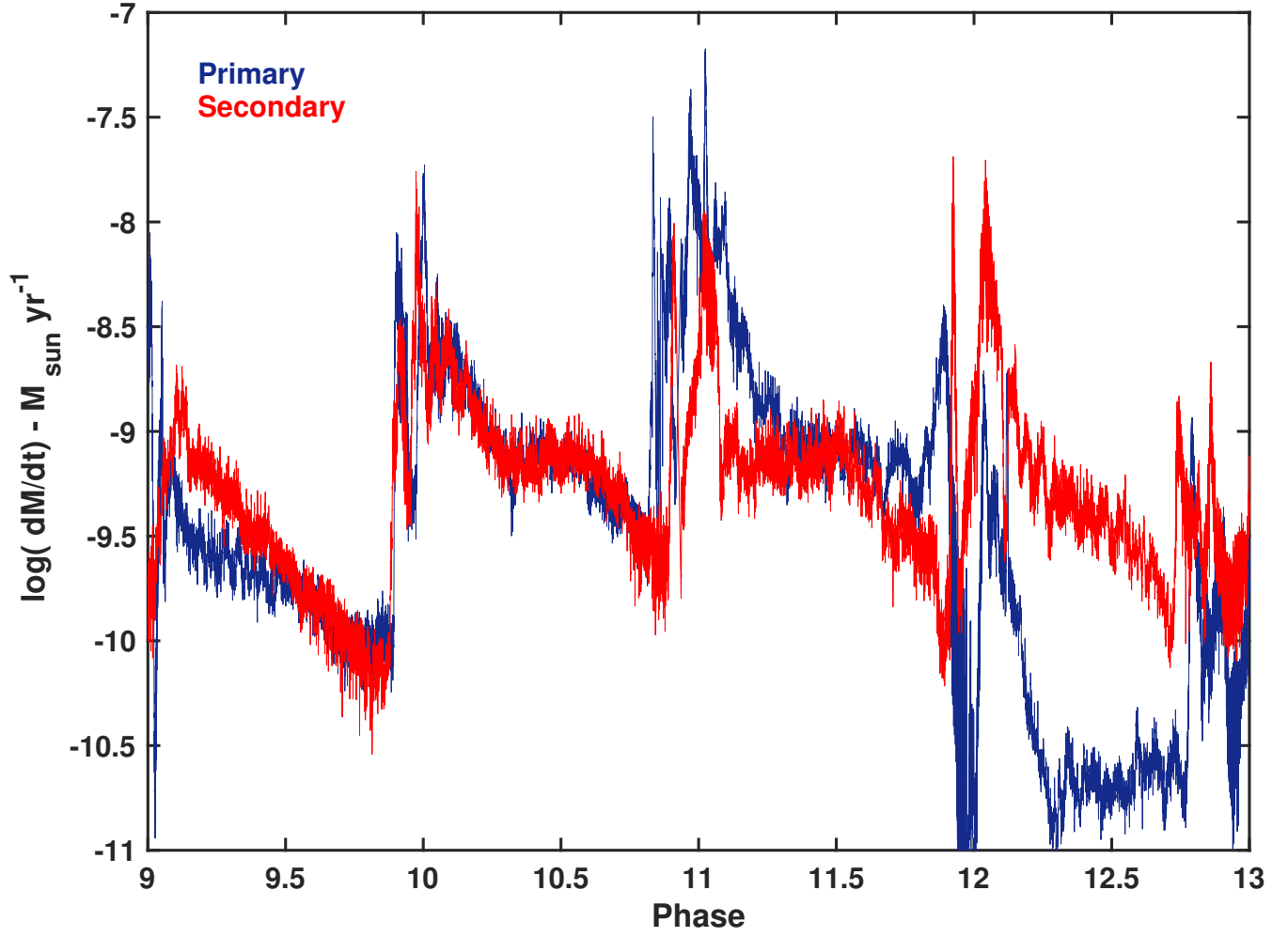


Fig. 17.— Expected accretion rate onto both components of the system as inferred from numerical simulations (Paper I).

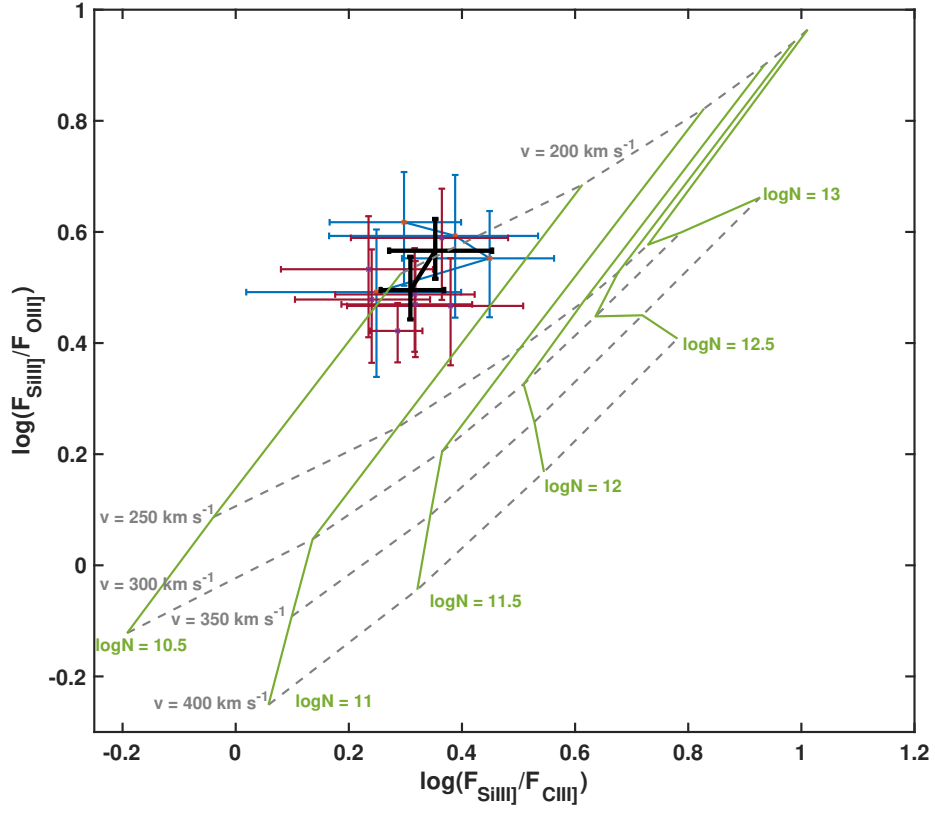


Fig. 18.— Accretion shock diagnosis diagram from Gómez de Castro & Lamzin (1999). AK observations during cycle 1 (blue) and 2 (red) are plotted in the diagram ( $1\text{-}\sigma$  error bars).

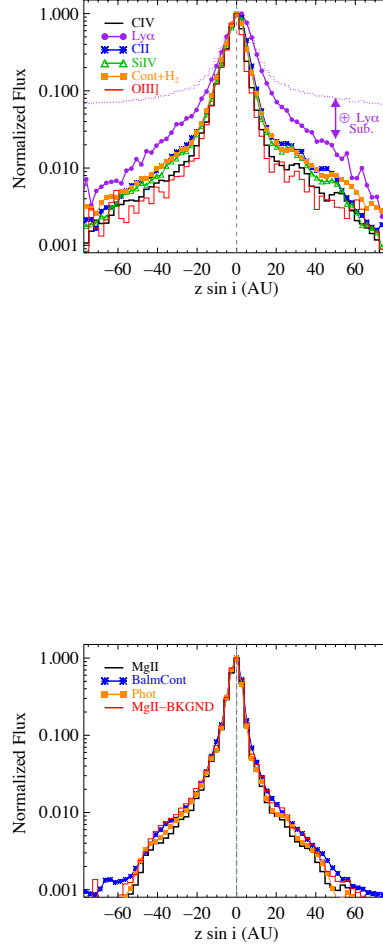


Fig. 19.— Spatial (cross-dispersion) profiles of the STIS G140L (*top*) and G230L (*bottom*) data in discrete bands, as labeled in the legends. The dotted and solid Ly $\alpha$  curves represent the Ly $\alpha$  extraction before and after subtracting the geocoronal signal, respectively.

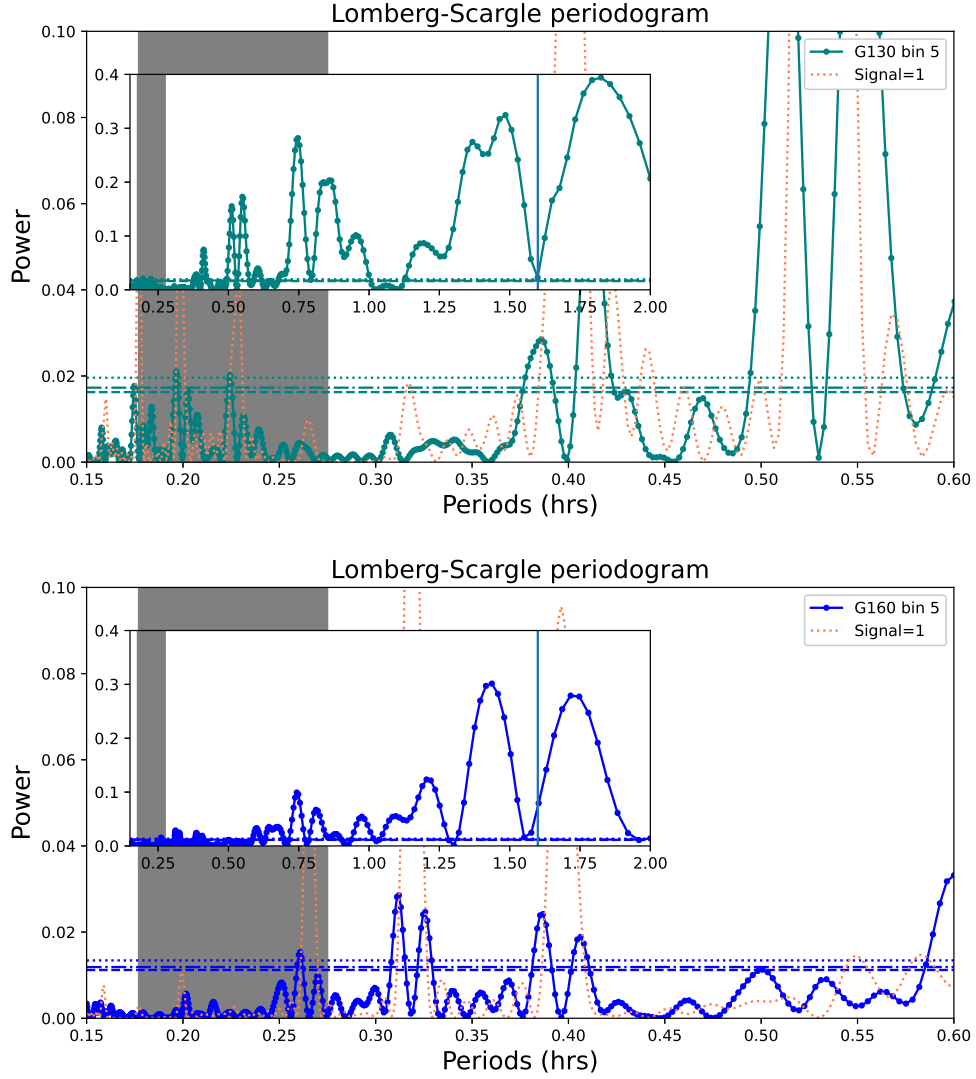


Fig. 20.— Lomb-Scargle periodograms corresponding to the COS light-curves. The upper panel corresponds to the G130M data, and the bottom panel to the G160M data. The grey areas show the suspected ULF period interval. The insets show the periodograms up to a period of 2.0hrs. The dotted pale curves result from processing the exposure signals arbitrarily set to 1, and follow the same patterns that the periodograms resulting from the real signal.

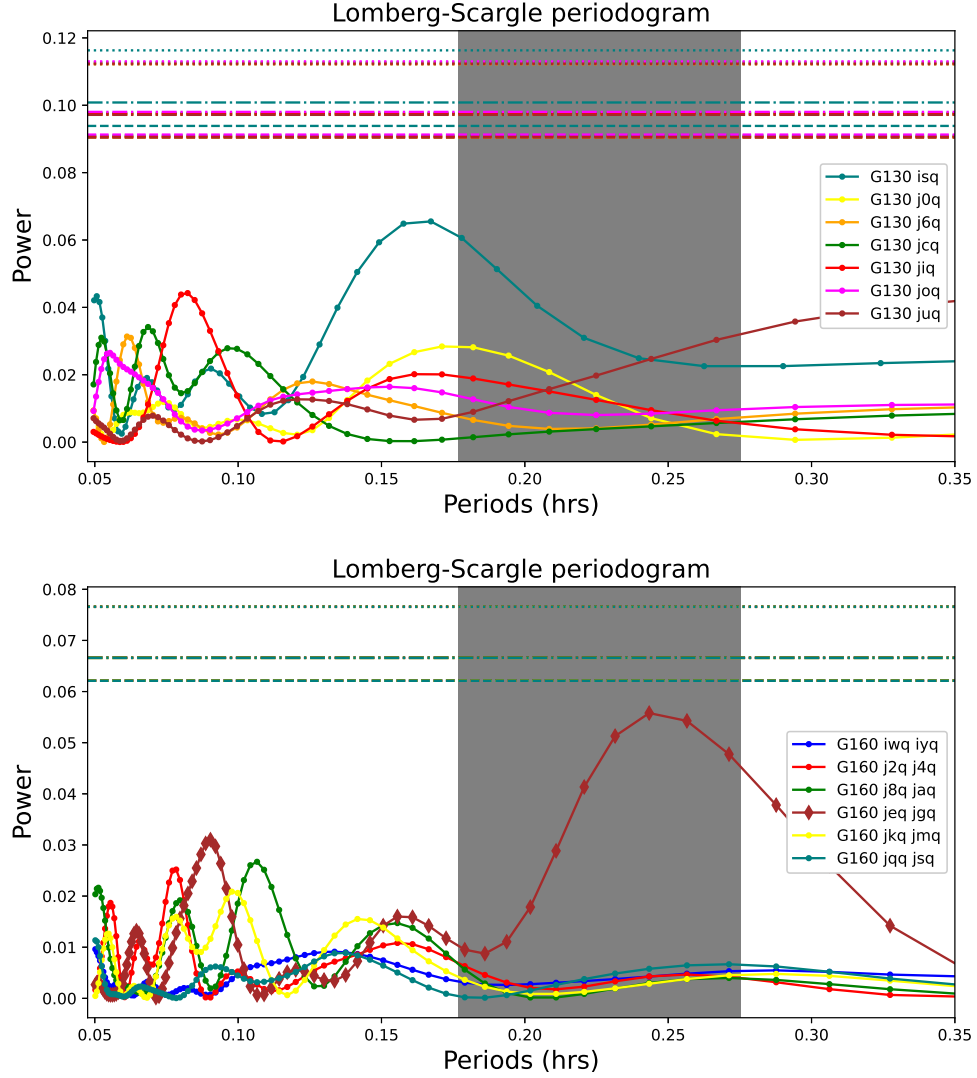


Fig. 21.— Lomb-Scargle periodograms corresponding to the G130M individual exposures (upper panel) and to the paired exposures from G160M data (bottom panel). The jeq-jgq pair presents a peak around 0.25hrs, with a fap of %24.

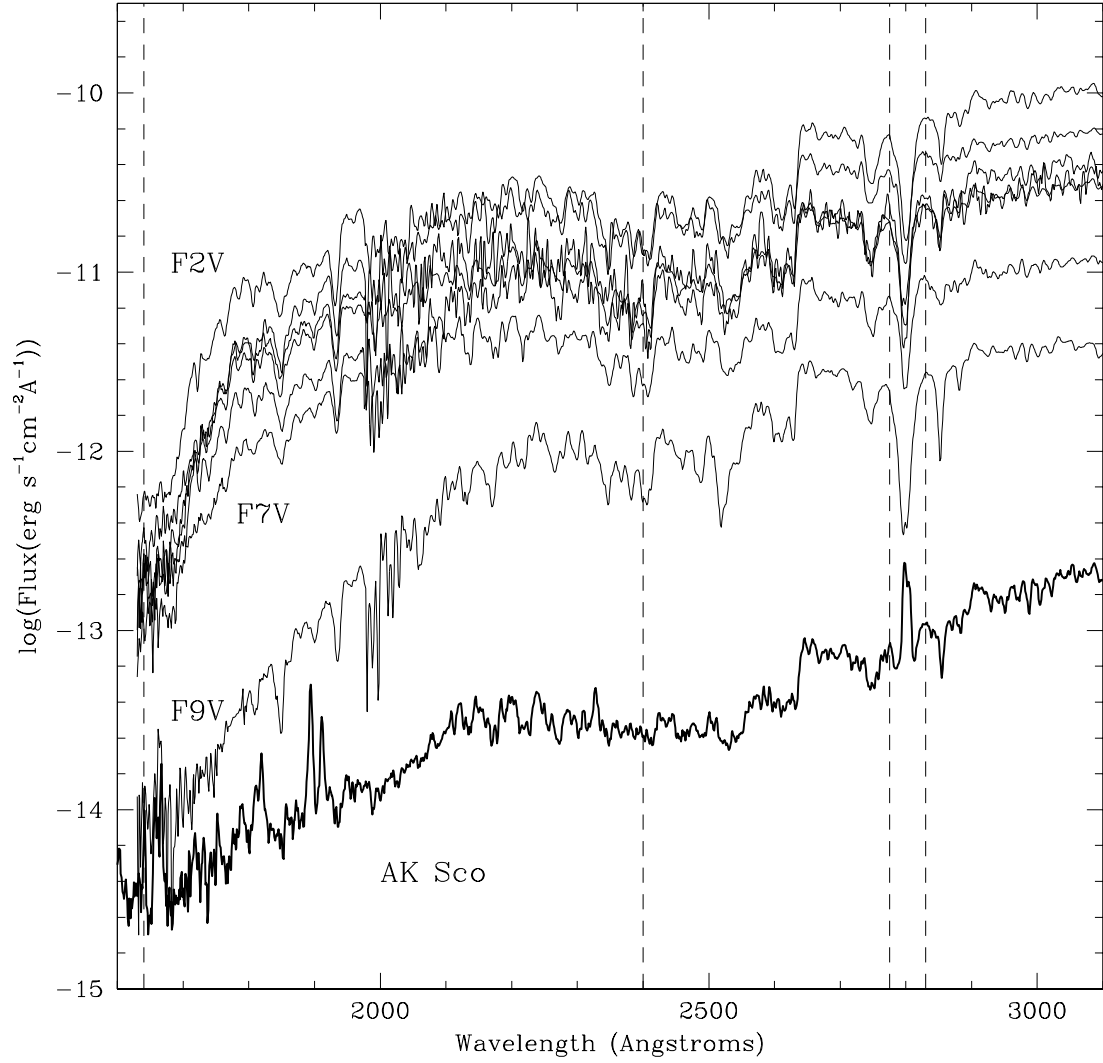


Fig. 22.— UV spectra of main sequence F stars. AK Sco spectrum is also plotted for comparison. The borders of the windows used to define the UV colour-colour diagrams are marked with dashed lines; note that the Mg II feature is avoided.

Table 1: AK Sco main parameters.

Property	Value	Source
Projected semimajor axis	$a \sin i = 30.77 \pm 0.12 R_{\odot}$	Andersen et al 1989
Eccentricity	$e = 0.47$	Andersen et al 1989, Alencar et al. 2003
Orbital period	$P = 13.609453 \pm 0.000026$ d	Andersen et al 1989, Alencar et al. 2003
Periastron Passage	$T = 2,446,654.3634 \pm 0.0086$	Alencar et al. 2003
Inclination	$i = 65^{\circ} - 70^{\circ}$	Alencar et al. 2003
Age	10-30 Myrs	Alencar et al. 2003
Spectral type	F5	Alencar et al. 2003
Stellar Mass	$M_* = 1.35 M_{\odot} \pm 0.07 M_{\odot}$	Alencar et al. 2003
Radius	$R_* = 1.59 R_{\odot} \pm 0.35 R_{\odot}$	Alencar et al. 2003
Projected rotation velocity	$v \sin i = 18.5 \pm 1.0$ km s <sup>-1</sup>	Alencar et al. 2003
Bolometric flux	$6.33 \times 10^{-9}$ erg s <sup>-1</sup> cm <sup>-2</sup>	Andersen et al 1989
$L_{bol}$	$8.07 L_{\odot}$	
Extinction: $A_V$	0.5 mag	Manset et al. 2005
Extinction: R	4.3	Manset et al. 2005
Distance	102.8 pc	Van Leeuwen 2007
Radial velocity	-1.3 km s <sup>-1</sup>	Gontcharov 2006

Table 2: Log of observations.

Instrument/ Grating	Observation ID	Start Time (JD-2456800.0)	Phase <sup>(1)</sup>	Exposure Time (sec)	Dispersion	Spec. Initial Wavelength (Å)	Spec. Final Wavelength (Å)
VISIT 1:							
STIS/G140L	OCA601010	47.740671	0.9924	1191.185	1190.000	1140.000	1730.000
STIS/G230L	OCA601020	47.760116	0.9939	716.200	740.000	1568.000	3184.000
STIS/G140L	OCA601030	47.799606	0.9968	600.179	1190.000	1140.000	1730.000
STIS/G230L	OCA601040	47.812211	0.9977	60.020	740.000	1568.000	3184.000
STIS/G140L	OCA601050	47.818565	0.9982	860.190	1190.000	1140.000	1730.000
STIS/G230L	OCA601060	47.834178	0.9993	50.002	740.000	1568.000	3184.000
STIS/G140L	OCA601070	47.865949	1.0017	600.193	1190.000	1140.000	1730.000
STIS/G230L	OCA601080	47.878553	1.0026	60.020	740.000	1568.000	3184.000
STIS/G140L	OCA601090	47.884907	1.0030	860.189	1190.000	1140.000	1730.000
STIS/G230L	OCA6010A0	47.900521	1.0042	50.002	740.000	1568.000	3184.000
VISIT 2:							
STIS/G140L	OCA602010	61.341238	0.9918	1191.198	1190.000	1140.000	1730.000
STIS/G230L	OCA602020	61.360683	0.9932	716.200	740.000	1568.000	3184.000
STIS/G140L	OCA602030	61.374630	0.9943	600.190	1190.000	1140.000	1730.000
STIS/G230L	OCA602040	61.414896	0.9973	60.020	740.000	1568.000	3184.000
STIS/G140L	OCA602050	61.421250	0.9977	860.184	1190.000	1140.000	1730.000
STIS/G230L	OCA602060	61.436863	0.9988	50.002	740.000	1568.000	3184.000
STIS/G140L	OCA602070	61.443102	0.9993	600.199	1190.000	1140.000	1730.000
STIS/G230L	OCA602080	61.474120	1.0016	60.020	740.000	1568.000	3184.000
STIS/G140L	OCA602090	61.480475	1.0021	860.197	1190.000	1140.000	1730.000
STIS/G230L	OCA6020A0	61.496088	1.0032	50.002	740.000	1568.000	3184.000
STIS/G140L	OCA6020B0	61.502326	1.0037	600.189	1190.000	1140.000	1730.000
STIS/G230L	OCA6020C0	61.514931	1.0046	60.020	740.000	1568.000	3184.000
STIS/G140L	OCA6020D0	61.540567	1.0065	860.199	1190.000	1140.000	1730.000
STIS/G230L	OCA6020E0	61.556181	1.0076	50.002	740.000	1568.000	3184.000
VISIT 3:							
COS/G130M	LCA603010	74.952778	0.9920	1000.192	19000.000	1159.478	1453.067
COS/G160M	LCA603020	74.967025	0.9930	1260.160	19000.000	1401.911	1762.490
COS/G160M	LCA603030	75.019109	0.9969	1600.320	19000.000	1416.649	1777.297
COS/G130M	LCA603040	75.041574	0.9985	1037.184	18000.000	1149.968	1443.513
COS/G160M	LCA603050	75.085498	1.0018	1600.288	19000.000	1428.748	1789.398
COS/G130M	LCA603060	75.108044	1.0034	1035.200	18000.000	1136.604	1430.194
COS/G160M	LCA603070	75.151852	1.0067	1600.384	19000.000	1428.846	1789.508
COS/G130M	LCA603080	75.174363	1.0083	1035.200	19000.000	1166.476	1460.058
COS/G160M	LCA603090	75.218194	1.0115	1600.384	19000.000	1410.898	1771.532
COS/G130M	LCA6030A0	75.240706	1.0131	1035.200	19000.000	1153.969	1447.576
COS/G160M	LCA6030B0	75.284560	1.0164	1600.320	19000.000	1405.080	1765.708
COS/G130M	LCA6030C0	75.307072	1.0180	1035.200	18000.000	1149.590	1443.174
COS/G160M	LCA6030D0	75.350903	1.0212	1600.352	19000.000	1419.522	1780.184
COS/G130M	LCA6030E0	75.373368	1.0229	1035.168	19000.000	1151.647	1445.254

(1) According to ephemeris in Table 1.

Table 3: F-type stars from the I.U.E. Archive<sup>(a)</sup>

Star	Spectral Type	Distance (pc)	(B-V) <sup>(b)</sup> mag
HD129502	F2V	18.3	0.37
HD26462	F4V	37.0	0.36
HD139664	F5V	17.4	0.40
HD22001	F5V	21.7	0.39
HD30652	F6V	8.1	0.44
HD173667	F6V	19.2	0.46
HD222368	F7V	13.7	0.50
HD126660	F7V	14.5	0.51
HD11007	F8V	27.9	0.55
HD114710	F9.5V	9.1	0.59
HD70907	F3IV/V	286.1	0.46
HD124850	F7IV	22.2	0.52
HD220657	F8IV	52.2	0.61
HD61110	F3III	51.0	0.40
HD57623	F6II	226.2	0.79
HD20902	F5Ib	155.3	0.48
HD171635	F7Ib	649.35	0.587
HD54605	F8Iab:	492.6	0.68

- (a) Spectral types, (B-V) and distances (parallaxes) have been extracted from the data base in the Centre de Données Stelaires in Strassbourg (France), using the SIMBAD interface.
- (b) Intrinsic (B-V) colours of main sequence F-type stars range from 0.32 (F0), 0.35 (F2), 0.45 (F5), 0.53 (F8) (source [www.stsci.edu/~inr/intrins/johnson.cols](http://www.stsci.edu/~inr/intrins/johnson.cols))

$$\langle v_{rad} \rangle = \frac{\frac{\sum_i \lambda_i F_i(\lambda)}{\sum_i F_i(\lambda)} - \lambda_o}{\lambda_o} c \quad (\text{A1})$$